

The Pulsation Characteristics of AH Camelopardalis: A Hot RRab with an Elusive Blazhko Modulation

S. M. Ward (& H. Petrovic)

L3 AstroLab, Department of Physics, Durham University

Observations: 17/10/18 - 03/12/18, Submitted: January 15th 2019

Physical properties of the RRab star AH Cam are studied, to better understand how the mysterious Blazhko effect can be modelled. 10 nights' photometric measurements from 17/10/18 – 03/12/18 yields 6 useful V-band peaks (& 03/12 companion B-band curve). With Durham Archive data and O-C considerations, optimised period of $0.368715(\pm 6)$ d and Blazhko period (11.0 ± 0.2) d is consistent with literature results ([1] [2] [3]). $\frac{dP}{dt} = (8 \pm 3) \times 10^{-10}$ d per cycle shows period evolves by $\pm 10^{-5}$ d over decade time-scales. A limited case study on the Blazhko modulation (§3.4) reveals the potential for deriving global Fourier parameters, as an alternative to the Baade-Wesselink IPM. With reddening corrections, mean temperature (7523 ± 82) K implies a hot RRab A9/F0 spectral class, with $(B-V)_0 = (0.29 \pm 0.01)$ mag near the instability strip 'blue edge' (~ 0.25). *Gaia DR2* [4] systematic uncertainties are identified, and Torres (2010) bolometric corrections [5] are deemed inapplicable to RRLs; corrected mean luminosity (34 ± 3) L_\odot and radius (3.4 ± 0.2) R_\odot are consistent with empirical trends [6]. (54 ± 18) min delay from R_{min} to L_{peak} affirms the κ mechanism [7] is the cause of fundamental pulsation. Retention of unique features in 'true' light curves, irrespective of fitting mode number, suggests hidden modes are unaccounted for. Our results support the beat frequency model of the Blazhko effect (Byrant (2015) [8]).

1. INTRODUCTION

RR Lyrae stars (RRLs) are a class of short period (0.2 - 1.1) d pulsating variables that are widely studied for their uses as standard candles, and as test subjects for stellar evolution and pulsation models [7][9]. Most often observed in globular clusters, they are low mass ($\sim 0.7 M_\odot$) Population II (metal-poor) main-sequence stars undergoing Helium to Carbon/Oxygen fusion in their cores, residing in the instability strip of the Horizontal Branch [10]. Limited to occupy this small region, RRL luminosity can be standardised [7]. Although stellar pulsations are not fully understood, it is accepted the " κ -mechanism" (§3.4), by which the opacity of ionised hydrogen/helium varies with temperature, plays a key role [11].

The Blazhko effect is a phenomenon exhibited in around half of RRLs [12] [13] (see Appendix A). Discovered over a century ago [14], this effect refers to a periodic modulation of amplitude and phase in RRL light curves. The exact physical mechanisms that give rise to this modulation, which we elaborate on in §3.4, remain unclear to this day [15]. Still, our continued study of the Blazhko effect is relevant, as a standardised period-luminosity relation for these stars has yet to be devised in the visible spectrum.¹ This means ground observations cannot yet effectively employ RRLs as standard candles.

However, with the recent *Gaia DR2* (Data Release 2, Apr. 2018 [4]) including observations of over 140,000 RR Lyraes [19][20], distance measurements derived from trigonometric parallaxes can be combined with observational data and empirical relations, that we might widely analyse RRLs in optical bands with ground observations.

Our goal is to determine the pulsation characteristics of the Blazhko RRab (Appendix B) AH Camelopardalis [21] (Table. I). We will use our results in tandem with Durham Archive data and the *GEOS* catalogue [3], to investigate

how the fundamental pulsation and Blazhko periods evolve, if at all, over decade timescales. Our observational data, captured over a period of approximately 8 weeks, will be used to construct light curves to determine fundamental period, Blazhko period, Temperature, Luminosity, Radius and Radial Velocity as a function of time. Our results will be compared with the *Gaia DR2* catalogue [4] and literature values of this well documented variable ([1][2][3][21][22]). Finally, overall conclusions will be drawn, regarding the rigidity of AH Cam's pulsation periods, and the consistency our data shares with stellar pulsation models of RRab stars.

In §2, we describe the choices made to maximise data precision, the efforts taken to quantify this precision, and the steps we take to construct our light curves. In §3, we determine pulsation periods and various other aforementioned physical parameters. A case study in modelling the Blazhko effect is presented also in §3.4. We discuss the systematic uncertainties and implications of our results, and suggest areas for future research, in §4, and finally, a summary of the key findings of this investigation is presented in §5.

2. METHODS

Observations of AH Cam from 17/10/18 - 03/12/18 are made with 4 telescopes located on the roof of Durham Physics Department (54.7670° N, 1.5740° W) [23] (see Table. I, VIII). Data from 10 nights includes 6 V-band light curve peaks, a companion B-band light curve observed on 03/12/18, and a variety of dark and flat frames captured for photometric purposes. Further details are in the Observing Log (Table. XI). For fine details of the telescopes and filter systems employed, see Appendix C.

2.1. Maximising SNR

When constructing AH Cam light curves, Signal-to-Noise Ratio (SNR) is the most important parameter in quantifying the precision of photometric measurements. High SNR (~ 100) yields low photometric errors ($\sim 1\%$), which is desirable when finely measuring the shifts in peak magnitude that result from the Blazhko effect. In general, a point source of light that spreads over p pixels, (described by a Gaussian Point-Spread Function) has an SNR described like

[1] Although period-luminosity-metallicity (PLZ) relations in the infrared spectrum have been employed successfully, with resulting distance uncertainties as low as 1% [16] [17], these are limited to the K-band. Our atmosphere emits heavily in IR [18], rendering these relations unworkable with ground observations.

so:

$$SNR = \frac{\sum_p S}{\sqrt{\sum_p (S + B + D + \sigma_R^2)}}. \quad (1)$$

Here, S , B and D are the signals in counts (ADU) recorded in a given pixel, from the target object, background sources, and dark current respectively. These signals are governed by Poisson statistics, due to the random and discrete nature of photon emission. The gaussian error σ_R is the readout noise: the standard deviation in the counts introduced by the charged-coupled device (CCD) following the exposure [18] [24].

Our atmosphere poses a multitude of challenges to overcome in seeking a high SNR: turbulence, absorption, and emission are but a handful of the processes that work against the ground observer to distort, displace and dilute the important photons we wish to analyse. In maximising SNR, and thus minimising magnitude errors, we must make informed choices wherever possible. Such freedoms to maximise SNR include choice of target, telescope, exposure time, aperture size and the application of flatfield corrections. Appendix C details also how SNR is maximised with the Temperature Control Function.

The freedom to choose a target gives us the opportunity to minimise X , the airmass. X is a dimensionless parameter, which describes how much atmosphere we observe our target through. In minimising airmass, we reduce the effects of atmospheric extinction and turbulence, caused by molecular absorption, Rayleigh scattering, and aerosol scattering, and in turn we maximise SNR [25].

$$X = \sec(z) \quad (2)$$

Eq. 2, derived from a simple plane-parallel atmosphere model, references the zenith angle z , measured between the zenith (the point directly overhead) and the target [18]. More complex models of airmass tend to the same limit for small z , and are thus surplus to our needs for modelling the atmosphere [25]. We choose a target as close as possible to the declination of our zenith: 54.767° . AH Cam declination is 55.500° , with a resulting airmass of $1.00008(\pm 1)$. Fig. 1 details how AH Cam RA is also well suited to our investigation.

In terms of telescope choice, we show no preference in this investigation. Of the four telescopes, all meet Nyquist's criterion for oversampling data; that the FWHM spreads across at least 2 pixels [26]. (average FWHM in Table. XI, pixel sizes detailed in [23]). Discrepancies in telescope diameter and pixel scale are unimportant given our 'relatively bright' target ($\sim 11 - 13$ mag).

In optimising exposure time for the B and V filters, we note SNR increases with exposure time [24]. However, the imperfections of our telescope target tracking are introduced if exposures are too long; indeed star trails become visible with 90s exposure frames. From Table. I, we note our target is dimmer in B than in V, thus requiring longer exposure times in the B-band. Employing GAIA software for quick photometric analysis, we find magnitude errors fall below ± 0.01 (photometric errors $\sim \pm 1\%$) for 30s and 60s exposures in the V and B bands respectively. We make no

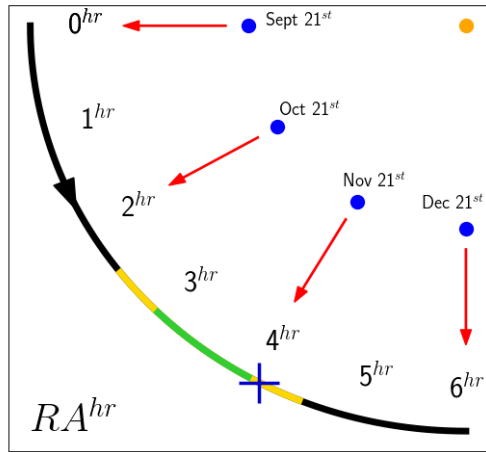


FIG. 1: Schematic shows the meridian Right Ascension (RA^{hr}) at midnight during observations, employed to determine optimum target RA. With an observation window from 15/10/18 - 07/12/18, and an estimated 8^{hr} FoV, we determine all targets within $(2.5 - 4.5)^{hr}$ [yellow] to be visible throughout each night, and claim $(3 - 4)^{hr}$ [green] is our optimum RA range. AH Cam, [blue cross] at $\sim 4.1^{hr}$, is suitable for our investigation.

effort to reduced magnitude errors further due to the reasons mentioned previously.

It is well known that aperture size has a bearing on SNR [26]. Apertures are the photometric tools we employ in GAIA, used to sum up counts within a circular region. The results of our aperture optimisation process, to maximise SNR, are shown in Fig. 2. We conduct flat-field corrections also, to account for the various imperfections of the telescope lens and CCD; the details of this process are laid out in Appendix D.

Finally, in Appendix E, we determine the gain and read-out of West-14 CCD to be $1.02713 \pm 0.00001 e^- ADU^{-1}$ and $12.6 \pm 0.08 e^-$ respectively. As Fig. 3 demonstrates, this means observations are signal and background noise limited, and so readout and gain characteristics of individual telescopes can be ignored. It is also shown that the automated subtraction of master-dark frames yields a bias-offset of zero, independent of exposure time. Thus, dark current and bias offset do not contribute to SNR.

2.2. Light Curve Construction

Construction of light curves such as in Fig. 4 requires photometric analysis, which we perform with various pre-conceived python scripts (Appendix F) and GAIA software. Having optimised all available freedoms governing SNR in §2.1, we describe now how light curves are constructed from a series of raw frames.

Magnitudes of point sources in GAIA are offset by an arbitrary value, denoted m_{zp} : the 'zero-point magnitude'. To derive apparent magnitude, we calculate this offset using Eq. 3.

$$m_{zp} = \frac{(m_1 - m'_1) + (m_2 - m'_2)}{2} \quad (3)$$

Here, subscripts denote discrete comparison objects of a

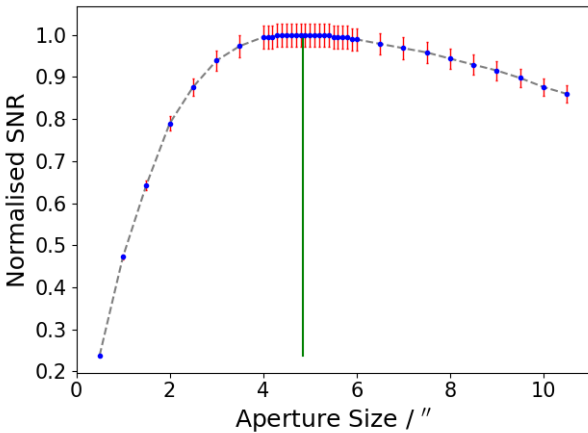


FIG. 2: SNR is plotted against aperture size in arc-seconds, to determine optimum GAIA aperture for AH Cam. Error bars have been scaled up by a factor 5 for clarity. Optimum SNR is found with GAIA by varying the radius of a circular aperture about AH Cam, in a 30s V-band frame. Excellent SNR suppresses magnitude error down to the minimum available number of significant figures. Thus the peak of this curve is flat in the range (4.3 - 5.4)”. The median value in this range: (4.85 ± 0.05) ”, is rounded up to accommodate for the limiting aperture increment of 0.1” in GAIA. Optimum aperture size for AH Cam is thus 4.9”

known catalogue magnitude m' , that we observe to have a magnitude m . This equation is powerful, as it allows us to factor in sky turbulence and cloud cover, which fluctuates unpredictably throughout a night’s observations (see Fig. 4, Table. XI).

To infer a magnitude offset of a target solely from measurements of comparison objects, necessarily, we require all objects considered to be influenced by the atmosphere in the same way. The ‘Fried parameter’, which describes the size of a pocket of air of constant density and temperature, quantifies this, but is non-trivial to calculate [18]. Appendix G lays out a simple argument as to why we cannot observe objects within one coherence length of one another. Qualitatively though, we desire comparison objects that reside as ‘close’ as possible to our target.

In addition, we are limited by our comparison objects’ brightness, which should be at least comparable to our target. This ensures companion object SNR is, as a minimum, comparable to target SNR, such that dominant errors from comparison objects are not unnecessarily introduced. With these limitations, there is little freedom of choice; our companion stars are showcased in Fig. 3 and Table. I.

With a known magnitude offset, and with CCD noise contributions neglected, magnitude and magnitude errors as a function of time are easily computed by iterating over raw frames, employing python scripts as described in Appendix F. Magnitude errors are derived with Eq. 4 [24], where SNR is as calculated in Eq. 1.

$$\Delta m = \frac{\log_{10}\left(1 + \frac{1}{SNR}\right)}{\log_{10}(2.5)} \quad (4)$$

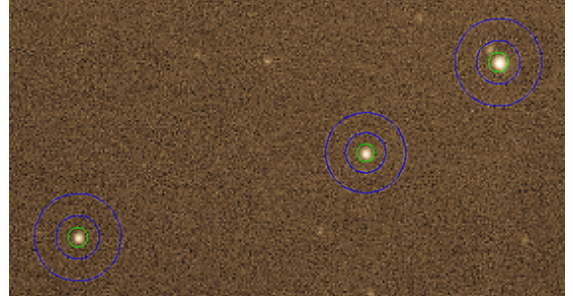


FIG. 3: GAIA screenshot displays, from right to left, our target star AH Cam, and comparison stars C1 and C2 (Table. I). Image spans approximately $310'' \times 74''$. AH Cam inner sky aperture is large enough to neglect contributions from companion star depicted next to AH Cam. Green aperture sizes are optimised at 4.9” to measure signal, typically of order ~ 5000 ADU per pixel. Blue Sky Apertures measure background noise, and are optimised at 11” and 23”. A typical sky noise value is ~ 500 ADU per pixel. By comparison with CCD noise quantified in §2.1, we conclude measurements are signal and background noise limited.

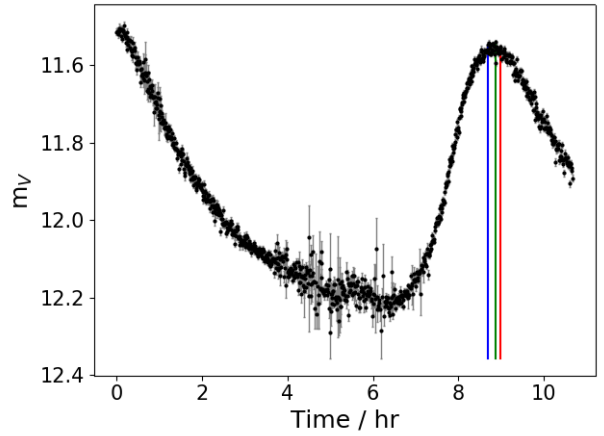


FIG. 4: V-Band light curve from 14/11/18 showcases several interesting features. Firstly, we note the Blazhko effect influences peak magnitude from period to period, where initial data points here clearly reside above peak magnitude by order ~ 0.1 mag. Secondly, we note the unpredictable nature of our observing conditions, where magnitude errors increase from an average of ± 0.01 to ± 0.02 in the range (4-7)hrs. Finally we draw attention to the 3-colour lines marking peak time and error either side. This is an example of a relatively large error in t_{peak} . See Table. VIII for t_{peak} and error values.

3. ANALYSIS

In this section, we lay out the processes employed to derive a variety of physical parameters, using the light curves constructed in §2.2. In §3.4 a case study on the Blazhko effect is detailed also. Firstly, we derive fundamental pulsation period and Blazhko period.

3.1. 2018 Data

The time of peak magnitude, t_{peak} , must be identified if we are to derive fundamental pulsation period, P . Firstly, the peak magnitude is identified. Next, the extreme times to either side of t_{peak} are determined, such that $m(t) - \alpha_{m(t)}$ is consistent with our peak magnitude and its associated error. (Formally, we subtract this error, given ‘peak’ magnitude is

TABLE I: UCAC4 catalogue details of our target star AH Cam, and the two comparison stars we employ for photometric analysis; denoted C1 and C2.

Name	UCAC4	RA ($^{\text{hr:mm:ss}}$)	Dec ($^{\circ} \text{ } '$)	m_V	m_B
AH Cam	728-031755	04 : 06 : 38.896	+55 : 29 : 59.48	11.562	12.251
C1	728-031772	04 : 06 : 45.492	+55 : 29 : 21.73	12.293	13.323
C2	728-031799	04 : 06 : 59.635	+55 : 28 : 45.72	12.775	13.297

in fact the minimum value m). An example of errors in time is displayed in Fig. 4.

With t_{peak} values extracted from 6 V-band light curves, P can be calculated as in Eq. 5:

$$HJD(t_{\text{peak}}) = kP + HJD_0, \quad (5)$$

where k is an integer number of cycles that have taken place since initial peak time, HJD_0 .

$$k = \text{round}\left(\frac{HJD(t_{\text{peak}}) - HJD_0}{P_{\text{approx}}}\right). \quad (6)$$

Our implicit assumption here is that P is rigid, allowing us to represent our findings as a straight line of constant gradient. This is, in general, a good assumption for RR Lyraes, and in §3.2 and §3.3, we demonstrate that this is valid for AH Cam. We adopt an estimated period $P_{\text{approx}} = 0.368\text{d}$ as is consistent with a variety of sources [1][2][21]. Using a reduced chi-squared optimisation technique in python (Appendix H), we determine optimum fit period and standard error. These results are displayed in Fig. 5 and Table. II.

Determination of Blazhko period, P_B , follows largely the same procedure as above: we fit peak magnitudes to a model function. By convention, we model our Blazhko Modulation with a single sine wave, comprising 4 free parameters, as in Eq. 7.

$$m(t_{\text{peak}}) = B_0 \sin(\omega_B t_{\text{peak}} + \phi_B) + B_1 \quad (7)$$

The Blazhko pulsation frequency is $\omega_B = \frac{2\pi}{P_B}$. The results of our χ^2_ν optimisation process are displayed in Fig. 6, and in Table. II and IX. Fig. 7 shows how the Blazhko phase of peaks is quantified by phase-folding data. §4 discusses the reliability of these results.

3.2. Durham Archive Data

CCD images captured by previous years' Astrolab students are stored in the Durham Archive; this provides us with an opportunity to examine the rigidity of AH Cam's period. We perform largely the same analyses as we do in §3.1, with some minor adjustments.

4 peaks are identified from 2012 data, as displayed in Table VIII. Flat-field frames are not stored in the archive, so we fashion our own. For a given telescope, we collect single frames of various targets in the V-band, captured within at least one month of the AH Cam observation. As a minimum, we stack 5 unique frames to create our master-flat; upon visual inspection of all master-flat frames, there are no unexpected point sources of light.

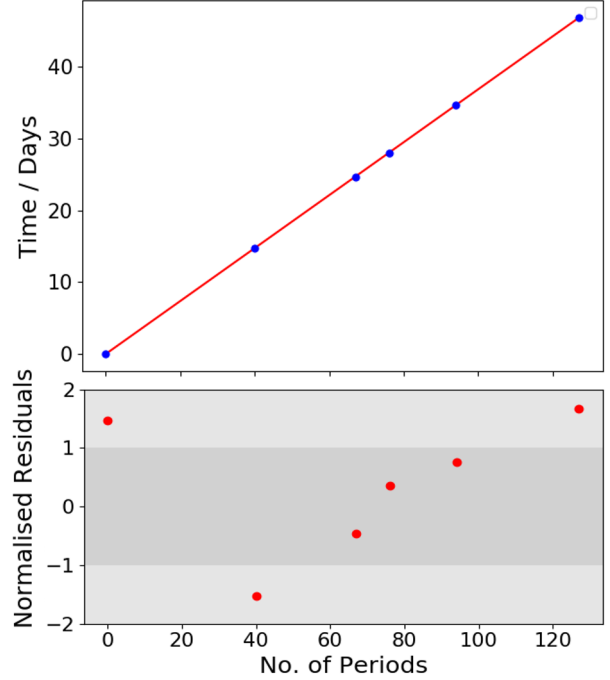


FIG. 5: 2018 peak times are plotted against cycle number, as in Eq. 5. Fundamental pulsation period in 2018 determined to be (0.36848 ± 0.00002) d. Linear fit of 6 peak times has $\chi^2_\nu = 2.05$ with half of all normalised residuals within ± 1 bounds. With only 4 degrees of freedom, we do not reject the null hypothesis, and conclude this is a good fit ($\chi^2_\nu \leq 2.9$ acceptable for $\nu \leq 5$ [28]).

From these 4 peaks, we determine the fundamental pulsation period of AH Cam in 2012 to be (0.3687 ± 0.0002) d, with a $\chi^2_\nu = 0.45$, and with all normalised residuals residing within ± 1 bounds. This implies an overestimation of peak time error bars. Although period is consistent with what we measure from 2018 data, by comparison, error in 2012 fundamental period is one order of magnitude larger, which is discussed in §4. Archive data graphs identical to those of Fig. 5 and 6 are displayed in Appendix I.

Limited to 4 peak values, χ^2_ν is undefined for 2012 P_B , as our Blazhko modulation model employs 4 free parameters. To remedy this, having determined optimum parameters, we re-run our chi-squared minimisation programme while holding one optimised parameter constant. In this case, we have only 3 free parameters and 1 degree of freedom, which yields a finite χ^2_ν and error α_{P_B} .

Of the free parameters available, holding phase constant yields the lowest error in Blazhko period (α_{P_B} ranges from ± 0.18 to ± 1.56). In all cases, χ^2_ν and P_B values are largely independent of the parameter held constant. (consistent χ^2_ν up to order 10^{-8} and P_B up to order 10^{-5}). Our results,

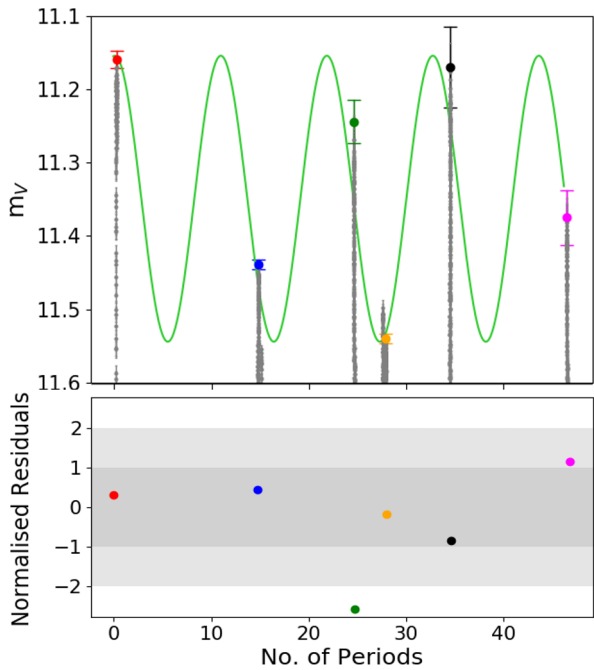


FIG. 6: Plot displays the 4-parameter sinusoidal fit we use to model the Blazhko modulation, laid over our data from 6 nights' observations in 2018. Blazhko Period determined to be (11.0 ± 0.2) d. Fit has a $\chi^2_\nu = 4.54$, with 2/3 of normalised residuals residing within ± 1 bounds. We reserve our discussion on the poor quality of this fit for §4.

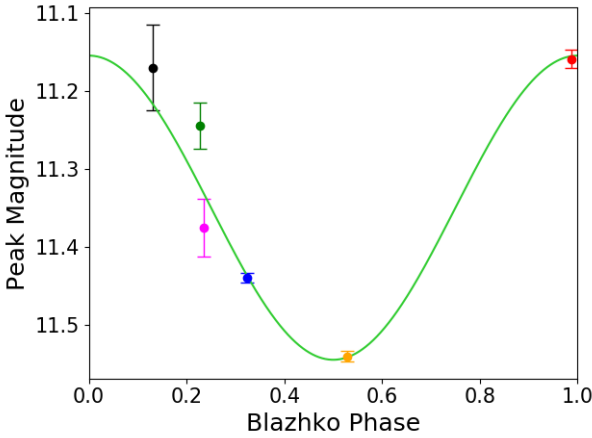


FIG. 7: Phase folded 2018 Blazhko data displays the Blazhko phases of peak magnitude data points as referenced in Table. VIII, and showcases the strong influences of sky noise on peak magnitude error (see Table. VIII). Blazhko Amplitude B_0 is (0.20 ± 0.02) mag. All Blazhko parameter data are displayed in Table. IX. 'Magenta' data from 03/12 is as close to a null modulation as we observe, with Blazhko Phase 0.236 ± 0.004 .

summarised in Table II, show Blazhko periods from 2012 and 2018 are consistent, with $P_B = (11.0 \pm 0.2)$ d.

3.3. Collated Data

In this section, we briefly contrast our results with research literature, and examine the rigidity of AH Cam fundamental and Blazhko periods. By comparison of several

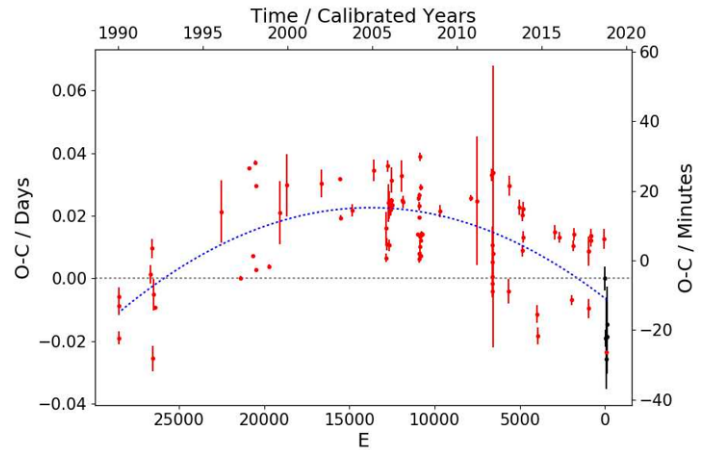


FIG. 8: O-C constructed from GEOS data [3] is fitted with a parabola as in Eq. 8 to infer period evolution (2018 observations in black). $\chi^2_\nu = 117$ implies a poor fit which is accounted for by the Blazhko effect. This modulation in phase shifts the peak time about the expected value [27], producing the scatter ($\sim \pm 0.01$ d) around the best fit line; for this reason, the poor χ^2_ν can be ignored. $\frac{dP}{dt}$ is measured to be $(8 \pm 3) \times 10^{-10}$ days per cycle. Period is optimised, by minimising the total deviation of points from the O-C = 0 axis, to be $0.368715(\pm 6)$ d, which is consistent with 2012 result only. At most, AH Cam fundamental period evolution is of order 10^{-5} d over decade time-scales. Applying $\frac{dP}{dt}$ from 2012 with optimised period, our 2018 derived result is not replicated. Thus natural period changes are not responsible for the inconsistency our 2018 P shares with literature.

AH Cam studies ([1] [2] [3] [21] [22]), we determine our measurements of P_B are consistent in all cases. It is typical of P_B measurements that uncertainties are of order ± 0.1 d, thus a description of Blazhko period evolution cannot be inferred from our datasets.

Conversely, fundamental pulsation period, P , is often recorded to several decimal places. In all cases our measured P is consistent with the literature to the first 3 significant figures (0.368 d). However, result inconsistencies emerge between literature values themselves, and our value, for significant figures ≥ 4 , which we discuss further.

An O-C diagram ('Observed minus Calculated' peak time) is used to measure the minute changes in period over decade timescales. Eq. 8 and Eq. 9 are taken from Sterken (2005) [29], and are used to infer this evolution, $\frac{dP}{dt}$. E is the number of cycles, and P is our measured value.

$$O - C = t_{peak} - \left(t_0 - \text{round}\left(\frac{t_0 - t_{peak}}{P} \right) P \right) \quad (8)$$

$$O - C = \frac{1}{2} \frac{dP}{dt} E^2 \quad (9)$$

Peak time data from the GEOS catalogue [3] is extracted, and we choose our epoch, t_0 , to be the time of our first 2018 peak observation (Table. VIII). P derived from 2018 data is first employed, and produces a nonsensical plot. The lines of steep gradient that we observe in the O-C imply only that P is incorrect, and in thorough disagreement with recorded data. Indeed, the selection of literature values listed above are inconsistent with this P .

TABLE II: Fundamental pulsation period, P , and Blazhko period, P_B , results from 2018 observations and 2012 archive data are consistent. Heliocentric Julian Day (HJD) is Julian Day observed in the Sun's frame of reference.

Data	$HJD(+2400000.5)$	m_V	$P(\pm\alpha_P)/d$	χ^2_ν	$P_B(\pm\alpha_{P_B})/d$	χ^2_ν
2018	58408.85793 – 58456.24790	11.16(1) – 12.52(4)	0.36848(2)	2.05	11.0(2)	4.54
2012	55963.83313 – 55991.93888	11.2(1) – 12.351(6)	0.3687(2)	0.45	11.0(2)	9.02

Conversely our 2012 period (Table. II) is consistent with literature up to 4 decimal places. Employing this value in the O-C instead produces a sensible plot which we can analyse. Period is optimised from 2012 P , and resulting O-C is displayed in Fig. 8.

In conclusion AH Cam period evolution is, at a maximum, of order 10^{-5} d over decade time-scales. 2012 period only is consistent with our optimised period $0.368715(\pm 6)$ d, and $\frac{dP}{dt}$ inferred from optimum fit cannot replicate the measured period from 2018 data. The systematic uncertainties that account for this inconsistency with literature observations are discussed in §4. In future, O-C analysis (Fig. 8) should be extended to quantify the shifts in period that result from the Blazhko modulation [27].

3.4. Pulsation Modelling

The remainder of this investigation is dedicated to deriving the physical parameters of AH Cam. In this section, we perform an isolated study, in search of 'true' light curves embedded in our observational signal. We investigate whether, by accounting for the Blazhko modulation, light curve Fourier parameters are constant over the duration of the Blazhko period, P_B . These parameters, utilised in variety of empirical equations, are intrinsically linked to the physical traits of RRLs [6][30]. Before utilising these equations though, we require a better understanding of pulsations, the Blazhko modulation and its influences.

As mentioned in §1, the κ mechanism is responsible for the fundamental pulsation. This mechanism requires a finely tuned internal structure to operate, which is why the instability strip occupies only a small region of the HR diagram [10][31] (§3.5). In general, the opacity of stellar material varies inversely with temperature, meaning higher temperature regions permit the flow of radiation. However, pulsations require a 'damming' mechanism to periodically store and release energy. RRLs occupying the instability strip bear 'partial ionisation zones' embedded at a critical radius, where the opacity of ionised helium varies in proportion to temperature. This means during compression, the flow of radiation is restricted by this high opacity ionised helium, allowing the build up of energy. As temperature grows, radiation pressure dominates ($P_{rad} \propto T^4$), and the energy is released. Stellar layers are propelled outwards causing an increase in radius. Temperature decreases, helium recombines reducing opacity, and the stellar layers fall back to start the cycle anew [7][32].

With regards to the Blazhko effect, research into its stubborn mysteries has amounted to a multitude of theoretical proposals. Among the leading theories, Gillet (2013) [13] suggests a cyclic growth and decay of a magnetic field acting on the outer stellar layers of RRLs is responsible for the Blazhko modulation. Another model put forth by Buchler & Kollath (2011) [33] describes a 9:2 resonant interaction of

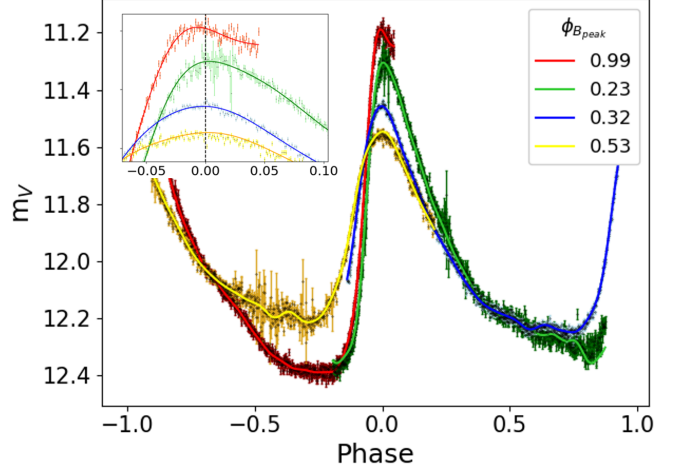


FIG. 9: The Blazhko Effect: fundamental period light curves are plotted, where amplitude and phase are modulated over the course of P_B [27]. Peak magnitude Blazhko phases are displayed in upper right corner. Spread in light curve peak magnitude is 0.38 ± 0.02 (all values in Table. VIII). Red peak of 10-mode optimum fit is offset by a phase -0.007 ± 0.001 , due to poor estimate of t_{peak} (see §4). RRab 'bump' features around phase $\sim \pm 0.7$ show no clear trend, and appear/disappear unpredictably (Appendix B). χ^2_ν for red, green, blue and yellow fits are (1.55, 2.00, 2.38, 2.73). §3.4 discusses these results further.

radial modes; flaws in this theory are pointed out by Bryant (2015) [8], who proposes instead that the Blazhko effect is the beat frequency of two near-frequency radial modes.

In all the models described above, properties such as metallicity, $[Fe/H]$ and mass are fixed [6]. These properties, as will be shown, are found with empirical equations and Fourier parameters. However, in observing a Blazhko modulated star, these parameters are modulated also, alluding to the false notion that metallicity and mass vary over P_B (mean M_V modulation is also amplified) [6]. The challenge here is to derive global Fourier parameters, independent of Blazhko phase, to derive meaningful physical results (see Appendix J on Baade-Wesselink IPM).

We perform a χ^2_ν optimisation process to determine the best fit parameters that describe our data (Appendix H). Adapted from [34], we employ the principle of superposition, modelling our light curves with i sine waves, each with a free amplitude and phase:

$$m(t) = m_0 + B(t) \left(\sum_i A_i \sin(i\omega t + \phi_i) \right). \quad (10)$$

The pulsation frequency $\omega = \frac{2\pi}{P}$ references the fundamental pulsation period that we measure in §3.1. The sum over i modes is our hypothesised 'true' light curve. A_i and

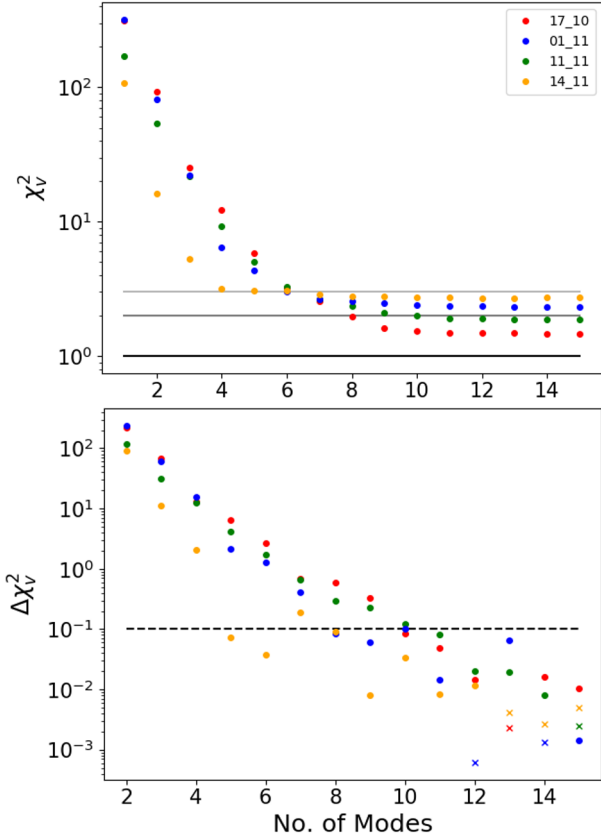


FIG. 10: Upper plot demonstrates variation in χ_{ν}^2 by fitting light curves from 4 nights' data (dates displayed in legend) with an increasing number of sinusoidal modes ($\chi_{\nu}^2 = (1,2,3)$ plotted for clarity). Plateau sets in around ~ 10 modes. Lower plot of $\Delta \chi_{\nu}^2$ ultimately indicates the 'improvement' to our fitting. ($|\Delta \chi_{\nu}^2|$ crosses indicate a worsening). Given an ideal $\chi_{\nu}^2 = 1$, and given errors in χ_{ν}^2 cannot be quantified, we decide a change of order 1 is a 'significant' improvement to χ_{ν}^2 . Conversely, we say a change of order 0.1 (dashed line) is an 'insignificant' improvement to χ_{ν}^2 . As displayed by lower plot, 11 modes onwards sees 'insignificant' improvements to all 4 datasets. Moreover, worsening to χ_{ν}^2 sets in for ≥ 12 modes. Thus, 10 modes are sufficient to describe our signals. χ_{ν}^2 values are displayed in Fig. 9.

ϕ_i are the Fourier amplitude and phase parameters. We insert a Blazhko modulation $B(t)$ into Eq. 10; this is a multiplicative factor that varies as a function of t/P_B :

$$B(t) = B_0 \sin(\omega_B t + \phi_B) + 1. \quad (11)$$

With no Blazhko effect considerations, Blazhko amplitude $B_0 = 0$ such that $B(t) = 1$. These fittings are the raw observational signals, whose constituent modes contain all the information that describe the Blazhko modulation, pictured in Fig. 9. By introducing a non-zero B_0 , we instead store this information in $B(t)$. We hope to compress signals observed at the peak of Blazhko modulation, and stretch signals observed at the minimum of Blazhko modulation, to yield a set of 'true' light curves that are consistent.

Analysis is performed on four nights' data that represent a diverse range over the Blazhko period: (Red, Blue, Green, Yellow data employed as in Fig. 9 and Table. VIII). Firstly, with $B_0 = 0$, we fit a number of modes in the range $1 \leq i \leq 15$, and investigate what number i best describes our

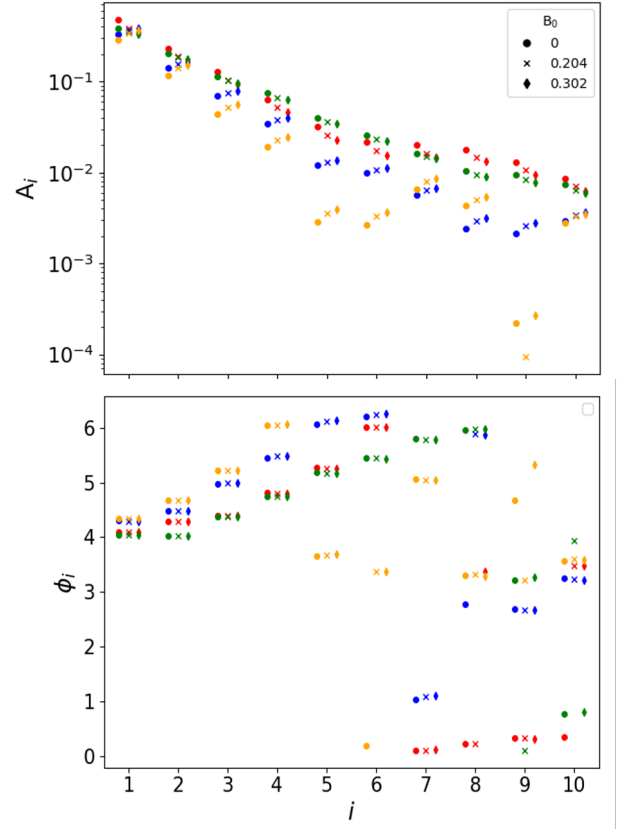


FIG. 11: Fourier amplitudes, A_i , and phases, ϕ_i , of 'true' light curves modulated by $B(t)$ are plotted for 10-mode optimum fits of 4 datasets. Upper right legend details the Blazhko amplitude B_0 employed in $B(t)$. Error bars not plotted for clarity. Appendix K details how we quantify improvement by measuring the change to RSD . On average, spread in A_i for the i^{th} mode improves by $(16 \pm 1)\%$ by employing $B_0 = 0.302$, whereas phases tend to worsen by $(-0.04 \pm 0.03)\%$. In all, Fourier amplitude consistency has a strong dependence on B_0 , whereas spread in phase values, limited to varying B_0 only, shows no such trend, and increases in the majority of cases.

data set. From Fig. 10, we determine 10 modes to be most suitable.

Next, we construct $B(t)$ derived from the 4 constituent peak magnitudes; this process is described in §3.1. With the free parameters of Eq. 7 determined, we re-run optimum fitting procedure with $B(t)$ (Eq. 11) in place, here with an amplitude (0.204 ± 0.007) mag.

Finally, we note the standard deviation of the peak magnitudes of 'true' light curves, and we optimise this standard deviation by varying amplitude B_0 only. This is done to a precision ± 0.001 in B_0 . From Fig 24, optimum $B_0 = 0.302 \pm 0.001$.

As Fig. 11 details, we find Fourier amplitudes are improved upon by changing $B_0 = 0$ to $B_0 = 0.302$, with an average reduction in A_i relative standard deviation of $(16 \pm 1)\%$. However, Fourier phase spread increases on average, by $(-0.04 \pm 0.03)\%$. Fig. 12 shows how individual nights' data retain unique features, implying the information that describes the Blazhko modulation has not been stored entirely in $B(t)$.

In all, we derive the following conclusions from this case study:

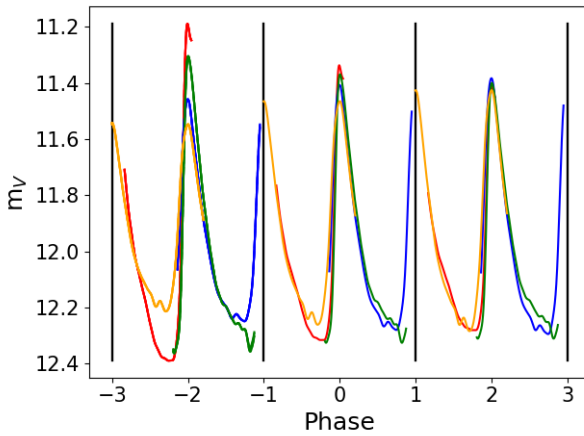


FIG. 12: Plot displays 'true' light curves. Left-hand plot shows best fitting to observational data with no Blazhko modulation (see Fig. 9). Centre plot is of 'true' light curves, that are modulated by $B(t)$ with $B_0 = 0.204$ to fit observational data, and right-hand plot is modulated with $B_0 = 0.302$ to fit observations. In fact, left-hand plot is an overlay of all these modulations, displaying the outputs of modulating left, centre and right graphs by their corresponding $B(t)$. Right-hand colour plots each retain unique features in regions of phase around minimum light, suggesting there are modes we have not accounted for in our analysis. Fig. 24 details peak magnitude standard deviation.

1) The existence of a single 'true' light curve, that is modulated in different ways by $B(t)$, cannot be ruled out. We have shown Fourier amplitudes tend towards consistency by varying B_0 , and we have limited our analysis to vary only 1 of 3 free parameters that describe $B(t)$ (Eq. 11). It is reasonable to suspect that varying Blazhko frequency, ω_B , and phase, ϕ_B , will also have a bearing on Fourier parameters; perhaps with further analysis phases would tend towards consistency also.

2) Contrary to **1)**, it seems there are fundamental differences between our 4 datasets. Indeed, Fig. 10 and Fig. 11 show explicitly that coloured datasets form distinct groupings. Visual inspection of Fig. 9 and Fig. 12, reveals the infamous RRab 'shoulder' or 'bump' (Appendix B) in 'yellow' data for example, but is clearly absent in 'red' data. If optimising other parameters as in **1)** is not sufficient to describe this, our $B(t)$ 4-parameter model needs modifying to account for hidden modes, that give rise to this elusive 'bump'. By extension, it may be the case our model as in Eq. 10 simply does not hold, and it is wrong to extend the Blazhko modulation we observe for peak magnitudes, to the entirety of the light curve observational dataset (more in §4).

3) The Blazhko modulation, $B(t)$, derived using §3.1 procedure, is heavily dependant on the peak magnitude data we employ. Table. IX displays $B(t)$ derived from §3.1 and §3.4 (6 and 4 nights' 2018 data respectively), showcasing the inconsistencies in Blazhko free parameters. §4 details further why such significant discrepancies emerge.

Results from this case study are inconclusive, and there is plenty of scope for further investigation, by varying all free Blazhko parameters, by encompassing all datasets and by testing more elaborate $B(t)$ models. For what remains of this investigation though, we employ standard procedure in determining Fourier parameters, by setting $B_0 = 0$.

3.5. Temperature

The RR lyrae instability strip is defined by the range of 'colour' or $(B - V)_0$ it occupies in the HR-diagram [31]. In theory there should be strict limits, however, just as our understanding of stellar pulsations is incomplete, there is controversy still in the typical range of RR Lyrae spectral classes: (Reference [35] A7 to F5, Reference [7] A2 to F6, Reference [10] A9 to F8). From spectroscopic studies, it is to be expected that throughout the course of a fundamental pulsation, an RRL will transition between at least 2 spectral classes [37].

The maximum mean temperature, referred to as the 'blue edge' of the instability strip, is often quoted to be of order 7500K (References $\sim 7400\text{K}$ [10], $(7550 \pm 270)\text{K}$ [31]). In all, we settle on a typical range in temperature of $(6500 - 7750)\text{ K}$, corresponding to a range in mean colour $\sim(0.25 - 0.5)$ (derived from Eq. 12) and spectral classes approximately A9 to F6. This is consistent with more recent findings [36].

Planck's law (Appendix L) dictates the shape of the black body spectrum, which depends only on temperature. In Ballesteros' recent study on black bodies (2012) [38], a relation between temperature and colour (B-V) in magnitudes is proposed:

$$T = 4600 \left(\frac{1}{0.92(B - V) + 1.7} + \frac{1}{0.92(B - V) + 0.62} \right). \quad (12)$$

From Fig. 4 and the extended discussion in §3.4, it is clear our data cannot be phase-folded reliably, given the difficulties in describing the elusive Blazhko modulation. Thus we require a simultaneous exposure in B and V bands to determine temperature as a function of time, which we capture on 03/12/18 ('Magenta' data Table. VIII). Spectral classes are taken from [35]. Each class is divided evenly into 10 subclasses (0-9) where lower numbers designate higher temperatures.

To calculate mean temperature, the average is taken over phase, limited from -0.5 to 0.5 for obvious reasons. In addition, we require equal weighting over this range. As is displayed in Fig. 13 and Fig. 14, uneven time spacing prevails due to failed astrometric fittings (that result from sky noise fluctuations). As such, our Fourier modelling code is employed to fit the data, which allows us to weight the curve evenly, and also reduce the effects of poorly measured data points, which can be seen around phase ~ 0.1 . Best fit-line in Fig. 26 Appendix M flattens out this noisy portion. Mean temperature $T_{eff} = (5255 \pm 35)\text{ K}$ corresponds to a cool spectral class: G6 (consistent with Gaia [4], Appendix N shows Gaia results are systematically offset).

Ignorance of interstellar extinction (Appendix O) yields temperatures below the expected spectral class range of RR Lyrae variable stars (see Appendix M for uncorrected temperature plots). This conclusion is consistent with the equivalent (B-V) magnitude (0.81 ± 0.01) , which is 'redder' than expected range by at least ~ 0.3 mag. In quantifying reddening, we employ empirical equations derived by Kovács and Walker (2001) [39].

$$(B - V)_0 = 0.209 \log P - 0.187 A_1 + 0.453 \quad (13)$$

With 'true' colour $(B - V)_0$ quantified, the reddening correction factor $E(B - V)$ can be determined, as in Eq. 14.

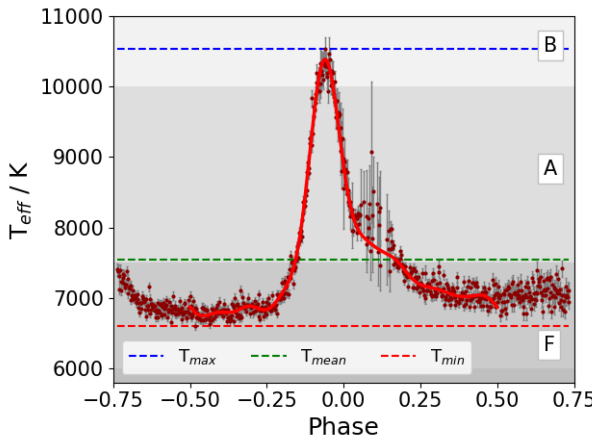


FIG. 13: Temperature results from reddening corrected 03/12/18 (B-V) magnitudes. Red fit-line plotted from phase -0.5 to 0.5 is implemented to give even weighting when averaging temperature, where failed astrometric fittings produce gaps in time around phase ~ 0.1 . Mean temperature, $T_{mean} = (7523 \pm 82)$ K, sits in A9 spectral class, and within uncertainty crosses boundary into F0 (note T_{mean} denoted at 7523K resides just above A9/F0 spectral class boundary at 7500K). T_{mean} corresponds to $(B-V) = (0.29 \pm 0.01)$ mag by Eq. 12. $T_{max} = (10537 \pm 166)$ K resides in B9 spectral class, $T_{min} = (6601 \pm 52)$ K rests precisely on the F5/6 boundary. Temperature range is thus (3936 ± 114) K. With mean spectral class at A9/F0 boundary, this represents a relatively hot RRL. Phase 0 is defined by light curve (Fig. 14); temperature peak is offset by (-0.061 ± 0.004) phase, where dominant systematic error arising from uncertainty in magnitude peak time is ignored.

$$(B - V) - (B - V)_0 = E(B - V). \quad (14)$$

Employing A_1 from m_V light curve fitting (Fig. 14, §3.6), $(B-V)_0 = (0.297 \pm 0.004)$ mag. Correcting $(B-V)$ mean magnitude from Fig. 26, $E(B-V) = (0.51 \pm 0.01)$ mag. Temperature is recalculated with the reddening constant extended to all (B-V) magnitudes, and is displayed in Fig. 13. Spectral class resides at A9/F0 boundary, matching our expectations for RRLs. Although peak temperature slips into B spectral class, as mentioned this is to be expected [37]. We conclude AH Cam is a hot RRab star, resting near the 'blue edge' limit of the instability strip.

3.6. Metallicity, M_V and Distance Constraints

As a precursor to calculating AH Cam luminosity, absolute magnitude in the V-band, M_V , must be determined. With Fourier parameters accessible, metallicity is also calculated, and by consideration of extinction, a constraint on the distance to AH Cam is tentatively applied to *Gaia*'s parallax measurement of (793 ± 21) pc [4].

Typical RRL M_V range is small, $\sim(0.4\text{--}0.8)$, due to the tight confinement in the instability strip [10] (in exceptional cases extends to $(0.3\text{--}1.0)$ [6]). In researching stellar evolution, mean metallicity of a globular cluster or elliptical galaxy is a powerful property to define. Since metallicity grows as a star undergoes fusion from lighter to heavier elements, metallicity is directly correlated with the time that has been permitted for stellar evolution [34]. Consequently,

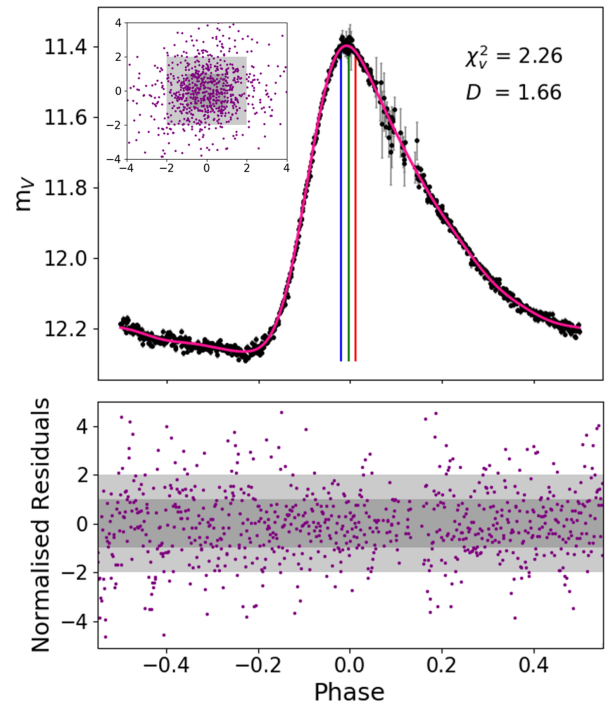


FIG. 14: 03/12/18 full phase V-band light curve is fitted with 7 sinusoidal modes (Appendix P). 3-colour lines indicate peak time and error (± 0.01 d). Lag-Plot is quantified by the Durbin-Watson Statistic. Optimised when $D = 2$, $D = 1.66$ suggests residuals are predominantly uncorrelated. With 53.6% of normalised residuals within ± 1 bounds, and $\chi^2_v = 2.26$, the null hypothesis is questioned but not rejected. The inclusion of background limited data points at phase ~ 0.1 limit the quality of this fit, however the further addition of modes would only improve fitting to these high error ($\sim \pm 0.05$ mag) data points, which is unphysical.

a globular clusters' constituent stars bear a unique range of metallicities, depending on its age. Metallicity is defined as $[Fe/H]$ in dex on the Zinn and West (ZW) scale [40], with RRLs typically ranging from -2.5 to -0.5 [31], where greater $[Fe/H]$ indicates a metal rich star. According to reference [9], there is no correlation between metallicity and Blazhko period, which is tested here, with the knowledge AH Cam P_B is atypically small.

Analysis begins with our modelling of the V-band light curve from 03/12/18. Employing the processes described in §3.4, 7 modes are used to model our light curve, by consideration of the reduced chi-squared statistic, χ^2_v , and the Durbin-Watson statistic, D . This is discussed further in Appendix P. Fig. 14 displays light curve fitting.

With Fourier parameters and associated errors quantified by means of χ^2 optimisation and the covariance matrix (Appendix H), Eq. 15 and 16 from references [30] and [41] respectively are employed to determine the metallicity, $[Fe/H]$ in the Jurcsik and Kovács (JK) scale, and mean M_V . Metallicity is converted to the ZW scale (Appendix Q).

$$[Fe/H]_{JK} = -5.038 - 5.394P + 1.345\phi_{31} \quad (15)$$

$$M_V = -1.876\log P - 1.158A_1 + 0.821A_3 + 0.41 \quad (16)$$

These empirical equations are derived from a specific

sample, so it is recommended the compatibility parameter be calculated [30], to determine if the equation is suitable for our target. We require $D_m < 3$, which is satisfied (see Appendix Q).

Results are: $D_m = 2.1 \pm 0.8$, $[Fe/H]_{ZW} = (-1.13 \pm 0.02)$ dex, $M_V = (0.887 \pm 0.001)$ mag. Absolute V magnitude is dim for an RRL, while metallicity here is around 1σ higher than typical metallicity ($[Fe/H]_{ZW} \sim -1.5 \pm 0.3$ dex [31]). An earlier work [1] that cites AH Cam as a metal-rich star ($\Delta S \approx -1.3$ approx. -0.4 in ZW scale), is consistent with our results only because errors are of order 200% in the ΔS scale [40]. Our results, with high precision $\sim 2\%$, are far more reliable, and challenge the notion that AH Cam is a particularly metal-rich star. It's more likely that AH Cam is a typically aged RRL ($\tau \sim 10 Gyr$ [31]). Our results affirm those of [9], as we have shown metallicity of AH Cam is typical even though Blazhko period is atypically short.

With mean absolute magnitude M_V determined, it is trivial to derive a distance to our target, provided we have the corresponding mean apparent magnitude, $\langle V \rangle$. We employ the method described in reference [42] to determine $\langle V \rangle$, where ΔV is simply the magnitude difference of maximum and minimum light. Errors are propagated trivially using Hughes and Hase [28].

$$\langle V \rangle = V_{min} - 0.375\Delta V - 0.04. \quad (17)$$

Distance estimate (1599 ± 9) pc is inconsistent with *Gaia* parallax measurements (Table. IV), with expected distance (793 ± 21) pc. Again, significant systematic uncertainties prevail because interstellar extinction has been neglected. Without the need for complex equations, *Gaia* distances are used to infer the V-band extinction, A_V .

$$A_V = \langle V \rangle - M_V + 5 - 5\log_{10}(D_{Gaia}) \quad (18)$$

$A_V = 1.52 \pm 0.06$, where errors are propagated trivially [28]. At this point, there is an opportunity to cross-reference our previously determined reddening constant (§3.5), with Eq. 19 from [43].

$$A_V = R_V \cdot E(B - V) \quad (19)$$

The typical Milky Way extinction law, with $R_V = 3.1$, is somewhat controversial, and formally, extinction maps such as in Schlegel (1998) [44] should be employed. Reddening is dependant on whether observations are made through diffuse or high density ISM [44], and the galactic position of AH Cam is not considered here.

$E(B-V)$ is determined to be (0.49 ± 0.02) , which is consistent with (0.51 ± 0.01) from §3.5 (and with findings from [1]). This gives us confidence in our quantification of reddening. Reverse-engineering this process, $E(B-V)$ from §3.5 is used in conjunction with Eq. 18 and 19 to determine distance. Due to the aforementioned reasons, our distance value is a prediction, and not a result based off of rigorous calculation.

Distance is determined to be (772 ± 24) pc. This is consistent with the lower bounds of *Gaia* parallax measurements, permitting the calculation of a weighted mean [28]. Our final distance value, based off of an extinction law with $R_V = 3.1$, is (784 ± 16) pc. Precision in *Gaia* measurement is therefore improved by $\sim 0.6\%$.

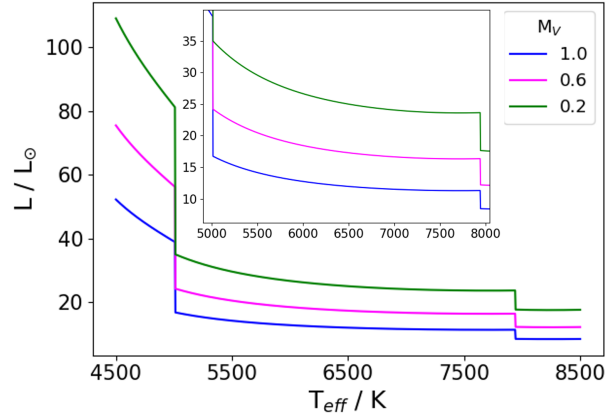


FIG. 15: A range of M_V values, in excess of what is typical of RRLs, are applied to the Torres (2010) bolometric correction system [5], and the resultant luminosities are plotted, with the expectation $L \sim (30 - 60) L_\odot$. Discontinuous boundaries of infinite gradient are those at $\log(T_{eff})$ equal 3.7 and 3.9 as defined by system. Range of luminosities in typical RRL temperature range are systematically offset from expectation by $\sim 30 L_\odot$, meaning this system should not be applied to RRLs, as it is incapable of replicating observations (more in Appendix R).

3.7. Luminosity, Radius & Radial Velocity

While temperatures boundaries of RR Lyrae are relatively well defined by the red and blue edges of the instability strip, there is more freedom in the allowed luminosity and radius. That said, empirical trends are clear; typical luminosities range from $\sim(30 - 60) L_\odot$ [6], and radius is typically $\sim(4-6) R_\odot$, with $\pm 1 R_\odot$ in rare cases. Pulsation amplitude velocities, here referred to as radial velocities (intrinsic to star), are typically $\sim 40 \text{ km s}^{-1}$, rarely in excess of $\sim 80 \text{ km s}^{-1}$ (references $\sim 60 - 70 \text{ km s}^{-1}$ [10], max 83 km s^{-1} in LMC survey [31]). Such measurements are imperative in testing pulsation models, and in analysing globular clusters (where GC velocity dispersion is derived from spectroscopic measurements).

To conclude construction of luminosity as function of time, a means of extending our V-band knowledge to all wavelengths is required. Bolometric corrections [5] (Appendix L) were applied according to our corrected temperature (Fig. 13), yielding M_{Bol} as a function of time. Employing $M_{Bol\odot} = 4.73$ as recommended in reference [5], luminosity is determined, and errors propagated [28].

From Planck's law (Appendix L), a powerful intrinsic relation between luminosity, radius and temperature is derived (Eq. 20). Assuming a sine series model of radius as a function of time (identical to Eq. 10), the radial velocity $RV(t)$ is the time derivative of $R(t)$, found with Eq. 21.

$$L = 4\pi R^2 \sigma T_{eff}^4. \quad (20)$$

$$RV(t) = \sum_i A_i i \omega \cos(i\omega t + \phi_i). \quad (21)$$

With L and T determined, it is trivial to calculate $R(t)$ and $RV(t)$, and propagate errors [28] (Appendix S). Results yield $L_{mean} = (12.5 \pm 0.9) L_\odot$ and $R_{mean} = (2.1 \pm 0.1) R_\odot$, which is highly unexpected, and cause for serious concern.

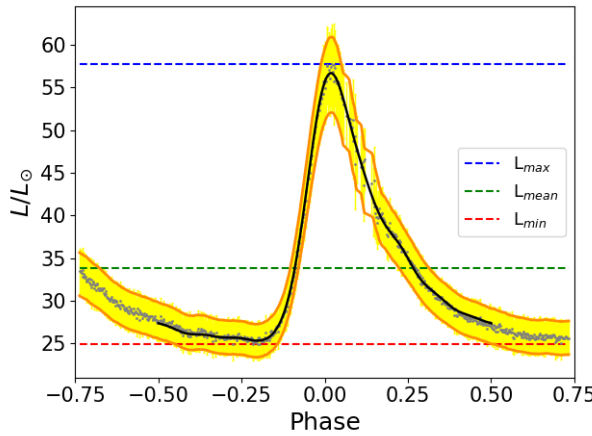


FIG. 16: Luminosity curve from 03/12/18 data, with smoothed upper/lower error bounds [orange], and best-fit line employed for averaging [black]. Peak luminosity is offset from m_V peak time by 0.018 ± 0.005 phase. $L_{peak} = (58 \pm 5) L_\odot$, $L_{mean} = (34 \pm 3) L_\odot$, $L_{min} = (25 \pm 2) L_\odot$. *Gaia* quotes a luminosity of $(10.3 \pm 1.5) L_\odot$, where 15% error is employed as suggested in reference [46]. As discussed in Appendix N, this inconsistent *Gaia* result is offset below expectations by at least $\sim 20 L_\odot$. Our corrected results are precisely what we expect, and by comparison with empirical trends, AH Cam is a dim RRab.

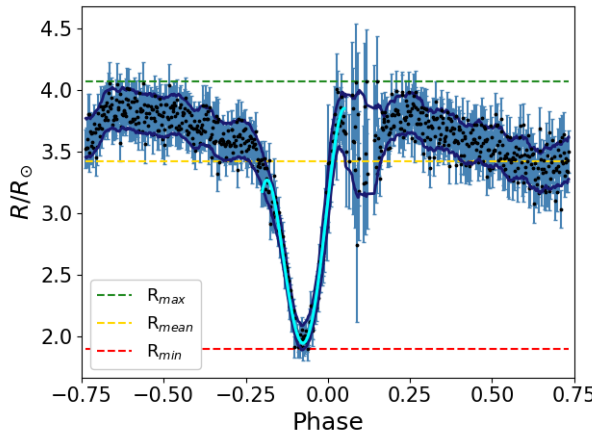


FIG. 17: Radius is plotted from 03/12/18 data. Error contributions from temperature and luminosity plots are compounded, producing a noisy plot; typical errors $\sim 0.2 R_\odot$ ('smoothed' error bounds fail to encapsulate error bars for this reason). 2-mode sinusoidal fitting [cyan] is employed over low error region to model radial velocity (see Appendix S). $R_{peak} = (4.1 \pm 0.4) R_\odot$, $R_{mean} = (3.4 \pm 0.2) R_\odot$, $R_{min} = (1.90 \pm 0.09) R_\odot$. Without a fitting applied from phase -0.5 to 0.5, R_{mean} is calculated without accounting for uneven time spacing of data points; on balance though, high errors at ~ 0.1 phase are countered by low number of data points. Minimum radius occurs at (-0.08 ± 0.03) phase. *Gaia* radius of $(4.5 \pm 0.4) R_\odot$ (10% error implemented [46]) is inconsistent with our results. As suggested in Appendix N, the absence of reddening considerations by *Gaia* is apparently responsible for the systematic uncertainty observed in temperature. If radius is inferred by *Gaia* from temperature and luminosity, these systematic uncertainties prevail, and account for the inconsistency with our results. In all, AH Cam is a particularly small RRab.

A thorough inspection of our procedure leads to an analysis of the bolometric correction system from Torres (2010) [5]. Fig. 15 shows this system is inapplicable to RR Lyrae stars, and a different system is required (see Appendix R for further details).

The bolometric correction as derived by Sandage and Cacciari (1990) [45] is employed with our metallicity derived from §3.6, and $M_{Bol\odot} = 4.75$.

$$BC_V = 0.06([Fe/H] + 1) \quad (22)$$

Results (Table. X) are far more reasonable, and are plotted in Fig. 16 and Fig. 17. $L_{mean} = (34 \pm 3) L_\odot$ and $R_{mean} = (3.4 \pm 0.2) R_\odot$ is aligned with expectations, and indicate AH Cam is a particularly small and dim RRab. Systematic uncertainties in these measurements are discussed further in §4. Peak phases (Table. X) affirm the κ mechanism is responsible for fundamental pulsation, with consistent timing of peak temperature and minimum radius, and a delay in peak luminosity of (54 ± 18) mins (details in Table. X).

Radius results are particularly noisy, and thus only a limited portion of the plot is employed to derive radial velocity (see Appendix S). Ultimately, RV results ($RV_{max} = (510 \pm 200) \text{ km s}^{-1}$, $RV_{min} = (-400 \pm 210) \text{ km s}^{-1}$, Fig. 36) are grossly over-estimated, featuring $\sim 50\%$ errors. Given the method, as described in Appendix S, is very much dependant on choice of modes and phase boundaries, and considering also our radius data is so noisy (see Fig. 34), it is not a cause for concern that $RV(t)$ is in excess of expectations; these results can be ignored.

4. DISCUSSION

In this section, attention is drawn to the significant inconsistencies our results show, such as the failure of 2018 derived fundamental period to match literature values, and the systematic inconsistencies in physical parameters we derive when compared with *Gaia*. Less significant systematic uncertainties that account for atypically small L and R by comparison with empirical trends are addressed also.

In deriving fundamental pulsation period, χ^2_ν code employs the uncertainty in peak time. As was shown in Fig. 9 [red], the Fourier modelling of our curves can peak at a phase *other* than zero. In essence: the peak time has been poorly estimated. Our method simply identifies the peak value and determines consistent extremities to either side. Clearly though, the peak data point can be unrepresentative of the local trend. In future, Fourier models should be applied *first*, then the peak of the smooth curve can be accurately identified. Where precision was previously dictated by sky noise (Table. VIII & XI), precision would instead be determined by Fourier parameter error (Appendix H). In addition, Blazhko influences on P ($\sim \pm 0.01$ d, Fig. 8) should be rigorously quantified, and factored into our analysis (As below, choice of data influences P).

In an effort to extend the Blazhko modulation of peak times to the entire light curve (and derive consistent Fourier parameters), several important findings are now discussed. Firstly, the choice of Blazhko peak data significantly alters the measured Blazhko period and other Fourier parameters in Eq. 11 (see Table. IX). It should be noted that this optimisation process (§3.1) accounts *only* for errors along 1

axis. Magnitude errors ($\sim 0.2\%$) which are included (Fig. 7) are dominant over errors in peak time ($\sim 0.03\%$). Yet in practice, choice of data impacts quality of fittings and results (Table. IX); this ultimately originates from systematic offsets in t_{peak} , which are excluded in the analysis. $\chi^2_\nu = 4.54$ and 9.02 arises because of poor t_{peak} estimation, and ignorance of Blazhko systematic error (as above and Appendix I), whereas overestimation of m_{peak} errors allows for too much freedom in the model function; $\chi^2_\nu = 0.33$ (remedied with Fourier fittings as above).

Secondly, we show in §3.4 that by varying Blazhko amplitude (Eq. 11), Fourier amplitudes tend towards consistency. There is ample opportunity here to extend this investigation, by varying Blazhko phase and period also, particularly if these parameters are derived from better fitting peak magnitude data (as above).

The optimisation of $B(t)$ can be extended beyond varying parameters of Eq. 11. As is discussed in §3.4 and Appendix B, Bryant [8] proposes the presence of near-frequency modes can replicate the RRab 'bump' that sometimes appears at phase ~ 0.7 . The addition of these modes to our 'true' light curve sum does *not* produce the desired effect, as is shown in Fig. 12, where curves retain their features, and as is determined by brief inspection of results derived from higher order modes (Fig. 10). Instead, extra modes should be added inside $B(t)$, or indeed outside of the modulated 'true' light curve term, to model the bump features (Fig. 9). Alternatively, a frequency spectrum should be taken to search for the presence of hidden modes (this was briefly attempted, but yielded unreasonable results).

Peaks are used to initially model $B(t)$, however, the troughs can also be considered in future if we desire to extend a modulation of peaks to the whole light curve. Is the trough modulation consistent with peak modulation? How do the Blazhko periods, amplitudes and phases compare? There is plenty of scope for further Blazhko modelling.

Moving on, the uncertainties in our physical parameters are now addressed. Firstly, *Gaia* results [4], are undoubtedly systematically offset (Table. IV), with temperature far cooler than the 'red edge' of the instability strip (§3.5), and luminosity far below empirical trends. A full discussion in Appendix N supports this, and we conclude, inconsistency with *Gaia* is not concerning.

All physical parameters were derived without Blazhko phase consideration (m_V peak Blazhko phase 0.236 ± 0.004), implying mean physical parameters differ from global parameters, which would be found with methods such as the Baade-Wesselink IPM that factor out Blazhko modulation (Appendix J). Nonetheless, this phase is as close as we observe to a null modulation (at phase 0.25 or 0.75, Fig. 7), thus, our parameters are a good approximation of the hypothesised global parameters.

In future, a thorough analysis of intrinsically constant physical parameters ($[Fe/H]$, mass) throughout the Blazhko phase should be conducted. As discussed in §3.4, any Blazhko effect model retains the notion that these are unchanged [6], yet, as depicted in Fig. 30, this is not what we observe. Perhaps the trends exhibited here can aid us in modelling the Blazhko modulation.

A potential source of systematic uncertainty, is that comparison stars are set to *UCAC4* catalogue values. The assumption here is that reddening and extinction effects are experienced indifferently by the three objects (AH Cam, C1, C2, Fig. 3). However, distance values from *Gaia* parallax

measurements [4] reveal this is not necessarily the case (see Table. VII for further details). In addition, it is assumed the filter bandpass and transmission spectrum used to measure catalogue values is the same as our telescope filter systems. This systematic uncertainty should also be quantified.

Finally, we draw attention to the finding that temperature is atypically large, while luminosity and radius are atypically small; our method is sensitive to a variety values, all of which can be systematically offset;

$[Fe/H]$: used in Bolometric Corrections [45], the measured value is dependant of Blazhko phase.

BC_V : Further to the above, this scheme is very simple, and perhaps outdated (1990) [45]. Unfortunately, as extensively discussed, the alternative Torres (2010) scheme [5] cannot be employed (Fig. 15, Appendix R).

$E(B-V)$: calculated twice (§3.5, §3.6), the former method was used in correcting temperature, as it avoids the use of extinction maps. It is sensitive to fundamental period, P , and Fourier parameter A_1 [39]. As shown (Fig. 11), Fourier parameters depend on Blazhko phase, and as extensively discussed, 2018 period is incorrect. However, 2018 derived P was employed, because O-C optimised period was derived only after completion of analysis.

Such a host of potential systematic uncertainties cannot be quantified, but with more time, these corrections should be implemented. It is likely temperature would be cooler (order $10^2 K$), and radius would be larger (order $1 R_\odot$), in alignment with empirical trends.

5. CONCLUSIONS

The associated periods and mean physical parameters of the RRab star AH Cam have been derived and studied, and scope for modelling the Blazhko effect has been narrowed. O-C considerations show natural changes to AH Cam period, of order $10^{-5} d$ over decade time-scales, do not replicate the findings of 2018 data analyses. Instead, 2018 derived period is systematically offset due to poor estimation of peak times. In future, Fourier models should be employed to determine peak time more accurately and precisely. Our best period estimate from O-C of $0.368715(\pm 6)$ d is consistent with period derived from 2012 Durham archive data, and other literature values ([1] [2] [3] [21] [22]). $P_B = (11.0 \pm 0.2) d$ is universally consistent.

$[Fe/H]_{ZW} = -1.13 \pm 0.02$ challenges the notion that AH Cam is an atypically metal rich RRL [1]. *Gaia* parallax precision is improved by 0.6%, with a weighted mean distance (784 ± 16) pc. Mean temperature resides in A9/F0 spectral class and indicates AH Cam is a hot RRab. Colour $(B-V)_0 = (0.29 \pm 0.01)$ is near the 'blue edge' of the instability strip (~ 0.25 , see §3.5). Mean luminosity and radius are small but consistent with empirical trends [6] [10], and systematic uncertainties are identified. It is shown *Gaia DR2* results [4] are systematically offset, and that the Torres (2010) bolometric corrections [5] should not be applied to RRLs.

Peak phase results support the κ mechanism as the cause of fundamental pulsation (§3.7, Table. X), and §3.4 shows consistent Fourier parameters of 'true' light curves may be attained with further analysis. Coupled with the retention of unique features irrespective of mode number, this suggests hidden near frequency modes as proposed by Bryant (2015) [8], perhaps stored in $B(t)$ or outside the modulated 'true' light curve term, may be responsible for the Blazhko effect.

Acknowledgments

Many Thanks to Dr Lucey, Dr Swinbank, and Ugne for all their help and guidance in the Astrolab, no matter what time of day! Thank you to all the Level 3 Lab Project staff members who have worked behind the scenes to help provide this well-oiled module. And of course thank you to Hannah, for being a knowledgeable, persistent, and patient lab partner, who has been a delight to work with.

References

- [1] Smith, H. A., et al. 1994, "AH Cam: A Metal Rich RR Lyrae Star with the Shortest Known Blazhko Period", AJ, 107, 2
- [2] Wils, P., Lloyd, C., Bernhard, K., 2006, "A catalogue of RR Lyrae stars from the Northern Sky Variability Survey", MNRAS, 368, 1757
- [3] GEOS RR Lyrae Datavase, URL: <http://rr-lyr.irap.omp.eu/dbrr/dbrr/> – V1.008.php?AH%20Cam, As of Dec. 2018
- [4] Gaia DR2 VizieR catalogue, URL: <http://vizier.u-strasbg.fr/viz-bin/VizieR-3?-source=I/345/gaia2>, As of Dec., 2018.
- [5] Torres, G., 2010, "On the use of Empirical Bolometric Corrections for Stars", AJ, 140, 1158–1162
- [6] Sodor, A., et. al 2009, "A new Method for Determining Physical Parameters of Fundamental Mode RR Lyrae Stars from Multicolour Light Curves", MNRAS, 394, 261
- [7] Kolenberg, K., 2012, "RR Lyrae Stars: Cosmic Lighthouses With a Twist", JAAVSO, Vol. 40
- [8] Bryant, P.H., 2015, "Is the Blazhko Effect the Beating of a Near-Resonant Double-Mode Pulsation?", ApJ, 802, 52
- [9] Jurcsik, J., et al 2006, "The Shortest Modulation Period Blazhko RR Lyrae Star: SS Cnc", AJ, 132, 61
- [10] Smith, H. A., 1995, *RR Lyrae Stars*, Cambridge University Press, Cambridge
- [11] Carroll, B. W., Ostlie, D. A., 2005, *An Introduction to Modern Astrophysics*, 2nd Ed, Willmann-Bell Inc., USA, pp. 541–561
- [12] Kovács, G., 2009, "The Blazhko effect", AIP Conference Proceedings, 1170, 261
- [13] Gillet, D., 2013, "Atmospheric dynamics in RR Lyrae stars", A&A, 554, A46
- [14] Blažko, S., 1907, "Mitteilung über veränderliche Sterne", Astron. Nachr., 175, 325
- [15] Kolenberg, K., et al 2009, "A photometric study of the southern Blazhko star SS For: unambiguous detection of quintuplet components", MNRAS, 396, 263
- [16] Monson, A. J., et al 2017, "Standard Galactic Field RR Lyrae. I.", AJ, 153, 96
- [17] Dambis, A. K., et al 2013, "RR Lyrae variables: Visual and Infrared Luminosities, Intrinsic Colours and Kinematics", MNRAS, 435, 3206
- [18] Swinbank, A. M., 2017, *Observational Techniques in Astronomy*, Durham University, UK, pp. 4–41
- [19] Holl, B., et al 2018, "Gaia Data Release 2; Summary of the variability processing and analysis results", A&A, 618, A30
- [20] Clementini, G., et al 2018, "Gaia Data Release 2; Specific characterisation and validation of all-sky Cepheids and RR Lyrae stars", preprint, (arXiv:1805.02079)
- [21] Goranskij, V.P., 1989, "Observation of the parametric resonance in AH Camelopardalis, an RR Lyrae-type star with the Blazhko effect", Astronomicheskii Zhurnal, Vol. 66, pp. 84–95
- [22] Smith, H. A., et al. 2002, "The Blazhko Effect of RR Lyrae in 1996", PASP, 115, 43
- [23] Department of Physics, Durham University, Astrolab Telescopes at Durham, URL: community.dur.ac.uk/physics.astrolab/atelescopes.html, As of Dec., 2018.
- [24] Raab, H., 2002, "Detecting and Measuring Faint Point Sources with a CCD", Astronomical Society of Linz
- [25] Green, D.W.E, 1992, "Magnitude Corrections for Atmospheric Extinction", International Comet Quarterly, Vol. 14, pp 55–59
- [26] Berry, R., Burnell, J., 1996, *The Handbook of Astronomical Image Processing*, Addison-Wesley Publishing Company, Inc., USA
- [27] Kolenberg, K., 2008, "What's New on the Blazhko Front", Phys.: Conf. Ser. 118 012060
- [28] Hughes, I.G., Hase, T.P.A, 2010, *Measurements and their Uncertainties*, Oxford University Press, Oxford, UK
- [29] Sterken, C., 2005, "The O-C Diagram: Basic Procedures", ASP Conf. Ser., 335, 3
- [30] Jurcsik, J., Kovács, G., 1996, "Determination of [Fe/H] from the light curves of RR Lyrae stars", A&A, 312, 111–120
- [31] Borissova, J., et. al 2004, "Properties of RR Lyrae stars in the Inner Regions of the Large Magellanic Cloud", A&A, 423, 97
- [32] Alexander, D., Stars, Stars & Galaxies Course, Level 2 Physics, Durham University
- [33] Buchler J. R., Kolláth Z., 2011, "On the Blazhko Effect in RR Lyrae Stars", ApJ, Vol. 731, pp. 24
- [34] Deb, S., Singh, H.P., et. al 2013, "Morphology and Metallicity of the Small Magellanic Cloud using RRab stars", MNRAS, 449, 3, 2768
- [35] Australia Telescope National Facility, Spectral Classes, URL: "http://www.atnf.csiro.au/outreach/education/senior/astrophysics/spectral_class.html", As of Dec. 2018
- [36] Sandage, A., 2006, "On the Predicted and Observed Colour Boundaries of the RR Lyrae Instability Strip as a Function of Metallicity", AJ, 131, 1750
- [37] Preston, G.W., 1959, "A Spectroscopic Study of the RR Lyrae Stars", ApJ, 130, 507
- [38] Ballesteros, F.J., 2012, "New Insights into Black Bodies", Europhysics Letters, Vol. 97, 3, pp. 34008
- [39] Kovács, G., Walker, A. R., 2001, "Empirical Relations for Cluster RR Lyrae Stars Revisited", A&A, 371, 579
- [40] Jurcsik, J., 2005, "Revision of the [Fe/H] Scales Used for Globular Clusters and RR Lyrae Variables", Acta Astronomica, 45, 653
- [41] Ferro, A.A., et. al 2012, "Physical Parameters of Three Field RR Lyrae Stars", Revista Mexicana de Astronomía y Astrofísica, 49, 1
- [42] Barnes, T. G., Hawley, S. L., 1986, "On the Absolute Magnitudes of RR Lyrae Stars", AJ, 307, L9–L13
- [43] Cardelli, J.A., Clayton, G.C., Mathis, J.S., 1989, "The relationship between infrared, optical, and ultraviolet extinctions", ApJ, 345, 245
- [44] Schlegel, D. J., et. al 1998 "Maps of Dust Infrared Emission for use in Estimation of Reddening and Cosmic Microwave Background Radiation Foregrounds", ApJ, 500, 525
- [45] Sandage, A., Cacciari, C., 1990, "The Abosolute Magnitudes of RR Lyrae Stars and the Age of the Galacite Globular Cluster System", AJ, 350, 645
- [46] Andrae, R., et. al 2018, "Gaia Data Release 2: first stellar parameters from Apsis", A&A, GDR2_Apsis
- [47] Bailey, S. I., 1902, "A Discussion of Variable Stars in the Cluster ω Centauri", Harvard College Observatory, 38, 1
- [48] Kolenberg, K., et al 2011, "Kepler Photometry of the Prototypical Blazhko star RR Lyr: An Old Friend Seen in a New Light", MNRAS, 411, 878
- [49] Flower, P. J., 1996, "Transformations from Theoretical Hertzsprung-Russell Diagrams to Color-Magnitude Diagrams: Effective Temperatures, B-V Colors, and Bolometric Corrections", ApJ, 469, 355
- [50] Theuns, T., Galaxies, Stars & Galaxies Course, Level 2 Physics, Durham University

APPENDIX A BLAZHKO STAR POPULATION DENSITY

The evidence is not clear as to how many RR Lyrae stars truly exhibit a Blazhko modulation, and figures may vary by order $\sim 20\%$ depending on the population under inspection. Reference [12] provides tables and further references showcasing the variety of findings concerning Blazhko modulated RRL population density.

APPENDIX B RRL SUBCLASSES

Bailey's original a, b and c subclasses of RR Lyrae [47] have since been revised following extensive research and data collection from the HST, the *Kepler* spacecraft and the *Gaia* satellite [19] [48]. AH Cam is an example of the most commonly observed RRab star, a fundamental mode pulsator, with a characteristic 'sawtooth' lightcurve [10], as is displayed in Fig. 9. RRc stars are first-overtone pulsators, which generally have a smoother, sinusoidal lightcurve. The final class are RRd stars (d: double-mode pulsator), bearing complex light curves, resulting from pulsations in both fundamental and first overtone modes [7].

An infamous feature of the RRab light curve is the 'shoulder' or 'bump' often observed near minimum light around phase ~ 0.7 . This 'bump' is known to appear, disappear, and move phase throughout the Blazhko cycle. Bryant [8] suggests this bump is a consequence purely of the additional mode "P02" which oscillates with frequency near to the fundamental pulsation mode.

APPENDIX C TELESCOPES, FILTERS & TCF

As of January 2019, 4 Telescopes in Durham Physics Department are Draco2, East-14, Far-East-16, and West-14, where number designation denotes telescope diameter in inches, excluding Draco2 which has a 14" diameter. In addition, 2012 Archive data observations are made with Draco (10") and West-12, as well as East-14. CCD is kept cool at a constant temperature of -10°C , which ensures dark current contribution is constant from night to night. This means dark-current subtraction can be automated, as is discussed fully in Appendix E.

All details regarding telescope focal length, pixel scale, plate scale, CCD's and filter systems can be found online at [23]. The 4 telescopes utilise either a QSI 583ws or a QSI 683ws Charge Coupled Device. Filters are imported from *Astrodon*.

The purpose of the Temperature Control Function (TCF) is to adjust the telescope focus in accordance with temperature, which fluctuates unpredictably throughout the course of a night's observations. Before a series of exposures are set running, the focus of the telescope is optimised to reduce the FWHM of our signal, and thus maximise SNR. The telescope focus is accurately controlled up to the order of micron length-scales. Given the metallic system is subject to thermal expansion and contraction at these length-scales, the python script governing the TCF adjusts the focus accordingly throughout the night, to maintain optimum seeing.

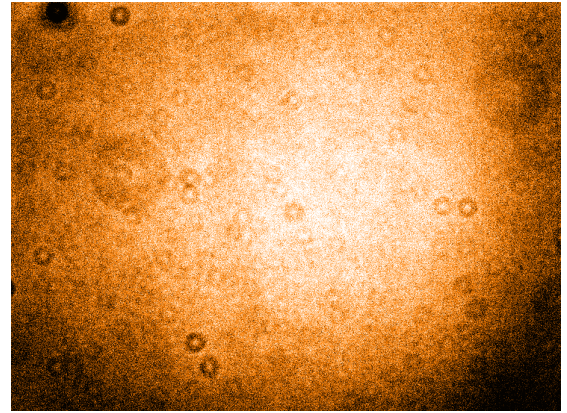


FIG. 18: Flat-field image clearly demonstrates the effect of vignetting, and the presence of lens imperfections, including 'dust doughnuts'. Flat-field corrections remove these features.

APPENDIX D FLAT-FIELD CORRECTIONS

We employ flat-field frames captured during twilight in the V and B bands, where exposure time is continually increased during the observing session, to counter the decreasing sky intensity. We aimed to fill pixels to half-well depth (2^{15}), as described in reference [26]. Twilight is chosen because it does not saturate pixels (unlike daylight sky) and is a uniform source (unlike night sky).

If a frame of a uniformly illuminated source is captured, there is a variation in intensity observed from the centre to the periphery of that frame. This is known as 'vignetting'. Flat-field corrections remove the effects of vignetting, 'dust doughnuts' and other blemishes on the lens; any variation in pixel sensitivity across the CCD is also accounted for [18]. Fig. 18 showcases these effects.

Multiple frames of a uniformly illuminated source are captured and stacked, and the median pixel values are extracted, to yield a master-flat frame. This frame divides the dark/bias subtracted image.

APPENDIX E CCD CHARACTERISATION

In quantifying magnitude errors associated with AH Cam (Eq. 1 and Eq. 4), we require knowledge of the parameters that characterise our CCD, specifically the readout noise and gain. GAIA's 'Fits Header' function suggests the readout and gain of all telescopes are consistent; $8 \text{ e}^{-} \text{ r.m.s}$ and $1.02 \text{ e}^{-}/\text{ADU}$ respectively. Using test frames captured by West-14, we measure these values experimentally.

To determine gain, flat field images in the V-band were captured at twilight, so as to fill pixels to half well-depth (2^{15}) [26]. For every pair of flat field images, a mean value was taken as the average pixel value in a box about the centre of a summed frame (100x100 pixels), and a variance value was taken as the squared standard deviation in the same box of a subtracted frame. The inverse gradient of variance against mean is the gain, as depicted in Fig. 19.

Readout noise is determined with a median dark frame, constructed from 32 minimum exposure (0.03s) CCD images, with the shutter closed. Each frame is subtracted from the median dark, and the standard deviation in a region about the centre is taken as σ_R . Readout noise is determined to be $12.6 \pm 0.08 \text{ e}^{-} \text{ r.m.s}$.

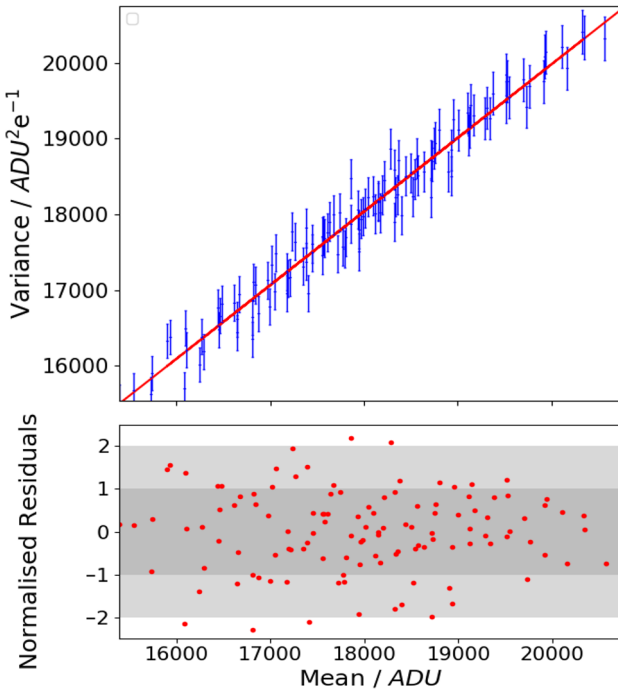


FIG. 19: Gain determined to be $1.02713 \pm 0.00001 \text{ e}^- \text{ADU}^{-1}$. Linear trend has $\chi^2_\nu = 0.87$, with 69.2% of normalised residuals lying within ± 1 bounds, implying optimum straight line parameters are an excellent fit. 16 flat field frames yield 120 data points.

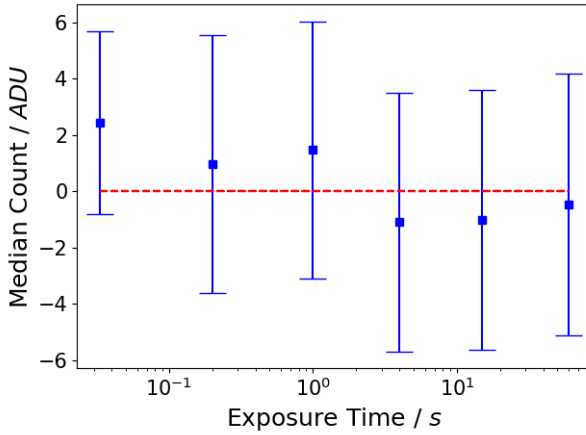


FIG. 20: Median count of master-dark-subtracted dark frames are consistent with a zero bias offset. Thus we have confidence in the automated subtraction of master-dark frames. Error bars account for readout noise, thermal accumulations during readout, and noise from unpatterned events. 32 frames of 0.03s exposures are used to calculate the first data point, whereas only 16 frames per exposure are used for the rest. Error bars are thus a factor $\sqrt{2}$ smaller for 0.03s data point compared to others (3.24 ADU and $(4.60 \pm 0.01) \text{ ADU}$ respectively).

Master dark images are automatically subtracted from raw frames to remove the contribution from dark current photons, that accumulate in direct proportion to exposure time. The removal of the bias offset, most often of order $\sim 100 \text{ ADU}$, is also automated. We run tests with already dark subtracted images to show explicitly whether this subtraction is performed accurately; a ‘successful’ dark/bias sub-

traction would yield an average of zero counts in a dark frame, independent of exposure time. Fig. 20 displays the results, that confirm a zero bias offset independent of exposure time.

As Fig. 3 in §2.2 details, we conclude observations are signal and background noise dominated, implying the individual CCD characteristics can be neglected, removing the need to quantify readout noise and gain for all 4 telescopes.

APPENDIX F PYTHON SCRIPTS

Dark frames are automatically subtracted from raw frames in accordance to their exposure time, and stored as `d.*.fits` files. An astrometric fitting is automatically applied to raw frames, to identify regions of the sky and assign *RA* and *Dec* angles. Successfully identified frames are stored as `ad.*.fits` files in the Durham Astrolab Database.

`automag_driver` contains a list of inputs including target and sky aperture sizes, readout noise, gain, and instrumental magnitude. We set aperture sizes to our optimum values as described in §2.1, and set readout and gain for all telescopes to be our measured values for West-14. Our gain value is consistent with all telescopes according to GAIA ‘Fits Header’ function, and sky and background noise limited observations means our choice of readout is submissive in the calculation of magnitude errors. Arbitrary instrumental magnitude is factored out during the light curve construction process.

`photom_ad2.py` iterates over `ad.*.fits` files, and applies the master-flat frame when provided by the user. This script outputs a `summary.obs` file, containing magnitude, magnitude errors, and Heliocentric Julian Day time of observations. Target and calibration star locations in degrees must be specified, and *UCAC4* catalogue is employed to extract catalogue magnitude values of calibration stars.

`raw2dif.py` acts on the `summary.obs` file to output light curves. We modify the code to apply Eq. 3, such that magnitude outputs are apparent magnitudes. We extract and save these light curves for analysis.

APPENDIX G FRIED PARAMETER

A typical coherence length for a good ground observation site would be of order $\sim 10 \text{ cm}$. We can approximate the ‘distance to our atmosphere’ to be somewhere in the range $10 - 100 \text{ km}$. Given this range, we are afforded at best, an angular separation on the sky of $\sim 2''$. As displayed in Fig. 3, comparison objects this close to AH Cam, and of comparable brightness to AH Cam, are not available to us.

APPENDIX H QUANTIFYING & OPTIMISING FIT QUALITY

To quantify the theoretical fit quality to a dataset, the reduced chi-squared statistic, χ^2_ν , is computed. Firstly, χ^2 is determined by summing the square of the normalised residuals:

$$\chi^2 = \sum_i \frac{(y_i - y(x_i))^2}{\alpha_i^2} \quad (23)$$

Here, subscript i denotes data points and errors, whereas the function $y()$ is the theoretical fit under scrutiny. When χ^2 is divided by the number of degrees of freedom, ν , χ_ν^2 is found. $\nu = n - N$, where n is the number of data points, and N is the number of free parameters that describe the model function, $y()$. In general, $\chi_\nu^2 = 1$ implies a perfect fit, $\chi_\nu^2 > 3$ is a poor fit, and $\chi_\nu^2 < 1$ implies errors α_i have been overestimated (exceptions to this for small ν detailed in [28]).

Often, errors in the free parameters that describe the model function are required. The covariance matrix is computed numerically, the diagonal elements of which represent the square of the parameter error. The computer program first derives the curvature matrix, A , which quantifies how the χ^2 statistic varies by changing free parameters. The elements of this matrix are [28]

$$A_{jk} = \frac{1}{2} \frac{\delta\chi^2}{\delta\alpha_j \delta\alpha_k}. \quad (24)$$

The inverse of the curvature matrix is the covariance matrix: $C = A^{-1}$. Finally, in the process of optimising a fit, computer minimisation techniques vary free parameters and compute the minimum χ^2 value. The associated free parameters are the 'optimised' parameters.

Normalised residuals, R_i , tell us information also about the quality of the fit. In general 65% of normalised residuals will reside within ± 1 bounds for a good fit, as will 96% within ± 2 bounds. When this criterion is not fulfilled, the fit should be inspected further.

In addition, there should be no structure to the normalised residuals, and should be dotted randomly above and below $R = 0$. The Durbin-Watson statistic, D , quantifies the structure of the normlised residuals.

$$D = \frac{\sum_{i=2}^n (R_i - R_{i-1})^2}{\sum_{i=1}^n R_i^2} \quad (25)$$

Optimised $D = 2$ implies normalised residuals are randomly distributed. $D = 0$ and $D = 4$ both imply significant residual structure, where respectively, residuals are correlated and anti-correlated with the model function. As with χ^2 , no error in D is quantified.

APPENDIX I ARCHIVE DATA RESULTS

Fig. 21 and Fig. 22 display the fundamental pulsation and Blazhko periods determined using 4 nights' data from 2012 Durham Archive. In both cases, results are consistent with 2018 observational data (see Table. II). A note on peak time errors is displayed in Fig. 23.

APPENDIX J BAADE-WESSELINK IPM

The Baade-Wesselink Inverse Photometric Method (IPM) is a tool to measure physical parameters of all RRL stars, regardless of whether they are modulated by the Blazhko effect or not [6]. The principle on which the method is founded, is that at points of equal colour on a

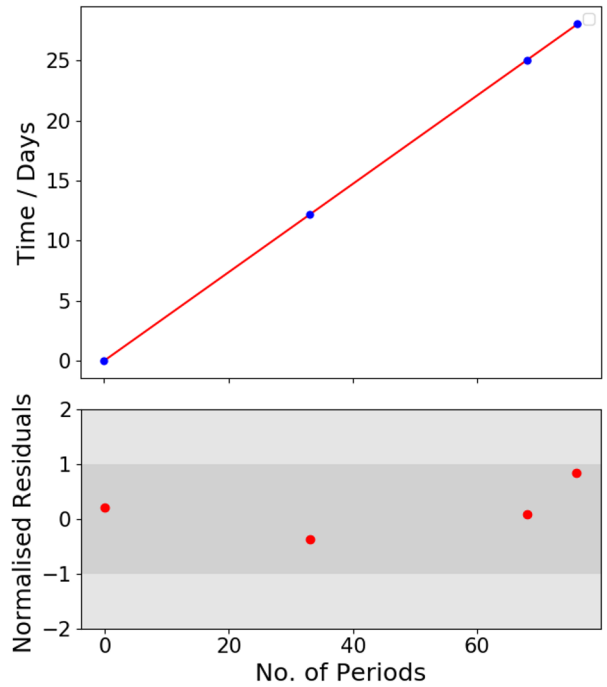


FIG. 21: Fundamental Pulsation Period determined to be $(0.3687 \pm 0.0002) d$. Linear fit of 4 peak times has a $\chi_\nu^2 = 0.45$ with all normalised residuals lying within ± 1 bounds, implying this is an excellent fit. By extension though, such a low χ_ν^2 with only 2 degrees of freedom implies data point errors have been overestimated. We discuss this further in §4.

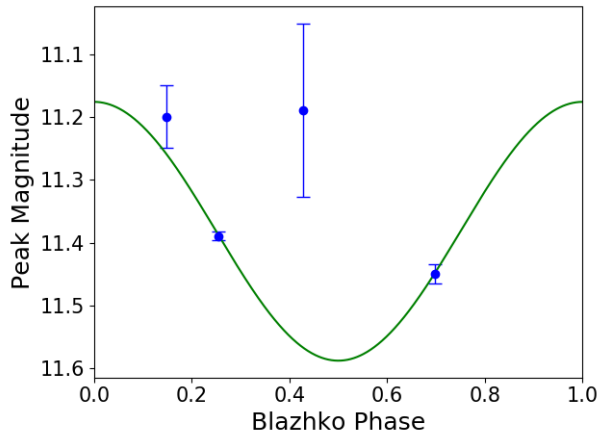


FIG. 22: Blazhko Period, P_B , from 2012 archive data is (11.0 ± 0.2) , $\chi_\nu^2 = 9.02$. Poor fitting data point arises from particularly noisy data, which is apparent upon inspection of 2012 light curve in Fig. 23.

light curve, the surface temperature is the same (Appendix L). Thus, any differences in magnitude can be attributed to radius.

This method is ideal for our purposes, however requires I-band light curves which we did not observe in. In future, a good test of 'true' light curve Fourier parameters (provided we yield a set of consistent Fourier parameters by extending §3.4), would be to compare physical parameter results with IPM results.

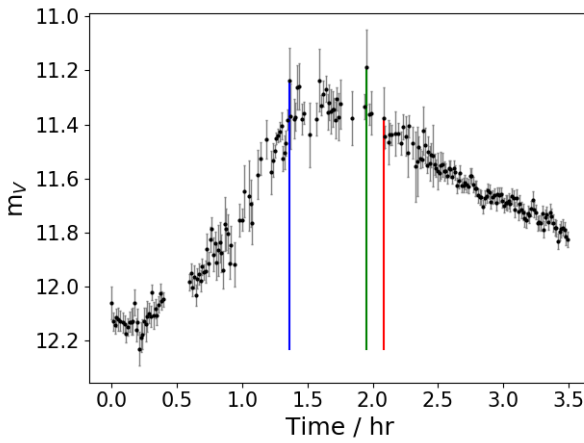


FIG. 23: Light curve yields poor fitting data point displayed in Fig. 22. Error in peak magnitude is 11.19 ± 0.01 , and peak time error is 0.03d, which is significant by comparison to other datasets (see Table. VIII). Poor fitting to Blazhko modulation of peak magnitudes can be attributed to background noise errors.

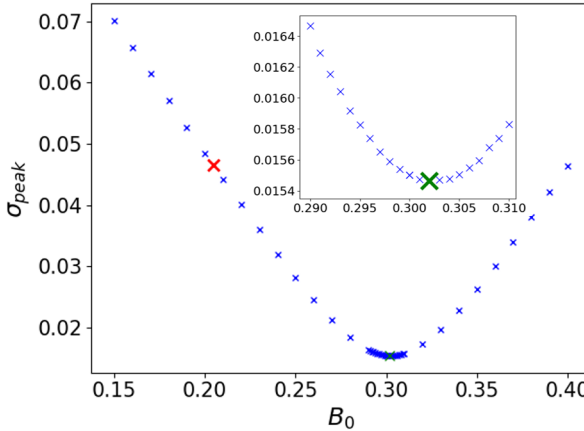


FIG. 24: Standard Deviation of 'true' light curve peak magnitudes is plotted for varying Blazhko modulation amplitude, B_0 . Red cross denotes $B_0 = 0.204$ determined by χ^2_ν optimisation of $B(t)$ in fitting peak magnitudes of 4 nights' data. Holding optimised $B(t)$ phase and frequency constant, B_0 is varied. Green cross is $B_0 = 0.302$ where standard deviation is minimised. All parameter values are displayed in Table. IX.

APPENDIX K PULSATION MODELLING

The Blazhko amplitude, B_0 , of the Blazhko modulation $B(t)$, is varied to minimise the standard deviation of 'true' light curve peaks, as displayed in Fig. 24. In varying B_0 , we find Fourier amplitudes of 10-mode fits become more consistent. Conversely, Fourier phase spread often increases. We quantify improvement with a measure of the Relative Standard Deviation (RSD), as described by Eq. 26.

$$RSD = 100 \times \frac{\sigma}{\mu} \quad (26)$$

RSD is a statistical parameter that describes the percentage spread of some data about a mean value. It compares the size of the standard deviation, σ , to the mean, μ , where the lower the RSD , the more tightly compact the data is about the mean. Improvement is defined as $RSD(B_0 = 0)$

- $RSD(B_0 = 0.302)$. The mean improvement and standard error is quoted in Fig. 11.

APPENDIX L PLANCK'S LAW & BOLOMETRIC CORRECTIONS

In 1900, Max Planck famously 'fudged' the black-body spectrum, and in doing so, was the first to quantise energy into the discrete packets we know today as photons. The spectral energy density, $B_\lambda(\lambda, T)$ [$\text{W sr}^{-1} \text{ m}^{-3}$], of a perfect absorber and emitter, in thermal equilibrium with its surroundings is

$$B_\lambda(\lambda, T) = \frac{2hc^2}{\lambda^5} \cdot \frac{1}{e^{\frac{hc}{\lambda k_B T}} - 1}. \quad (27)$$

For a given T , the flux observed in a given band occupies varying portions of the total bolometric flux (Fig. 25). Thus bolometric corrections are a function of T only.

Torres (2010) [5] prints corrected versions of bolometric corrections derived in Flower (1996) [49].

$$BC_V = a + b(\log T_{eff}) + c(\log T_{eff})^2 \dots \quad (28)$$

Constants are listed in Table. III. Erratic changes occur if T is treated as a function of time, as $\log T_{eff}$ crosses the 3.9 boundary. We choose the BC scheme to be fixed, determined by the mean temperature. $\log T_{mean} = 3.876 \pm 0.002$, thus only central column in Table. III is employed. With bolometric corrections in place, bolometric magnitude is trivially calculated.

$$M_{Bol} = M_V + BC_V \quad (29)$$

There is ambiguity in how errors are propagated, where constants associated with BC_V are excessively large by comparison to magnitude values. As it is not made clear in Torres (2010) [5], BC_V is taken to have no error contribution. Ultimately though, these corrections are not employed (Appendix R).

TABLE III: Bolometric correction system from Torres (2010)[5].

Constant	$\log T_{eff} < 3.7$	$3.7 < \log T_{eff} < 3.9$	$> \log T_{eff}$
a	-0.190537e5	-0.370510e5	-0.188115e6
b	0.155145e5	0.385673e5	0.137146e6
c	-0.421279e4	-0.150651e5	-0.636234e5
d	0.381476e3	0.261725e4	0.147413e5
e	0	-0.170624e3	-0.179587e4
f	0	0	0.788732e2

APPENDIX M TEMPERATURE, BUMP & PEAK

Displayed are the temperature results that are uncorrected for interstellar reddening. Fig. 26 and Fig. 27 differ only by the shape of the red fit-line near phase ~ 0.1 . Plot description discusses the presence of the bump. Finally, with consideration of sources that describe temperature and colour range of the instability strip [10][31][35][38], it appears reference [7] has misprinted the expected spectral class range to be A2 to F6.

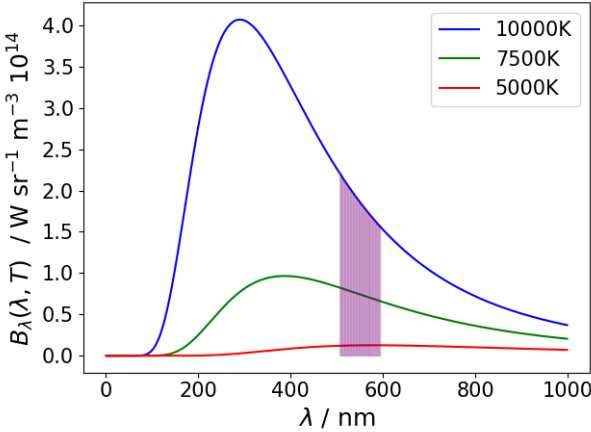


FIG. 25: Black-Body curve plotted for 3 temperatures. Purple shaded area indicates the approximate wavelength range we might expect for a V-band filter. Indeed, this area, corresponding to the flux we observe in the V-band, occupies a different proportion of the total area of each plot (F_{bol} by rearranging Eq. 20). Thus, bolometric corrections are required to extend V-band observations to bolometric quantities.

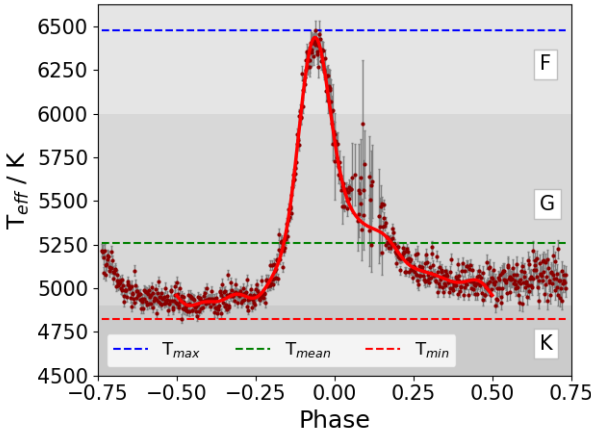


FIG. 26: Temperature results from uncorrected 03/12/18 (B-V) magnitudes. Red fit-line plotted from phase -0.5 to 0.5 is implemented, as discussed, to account for failed astrometric fittings. Mean temperature, $T_{eff} = (5255 \pm 35)$ K, resides in G6 spectral class: one class cooler than what is expected of typical RRLs. This corresponds to $(B-V) = 0.81 \pm 0.01$ by Eq. 12. $T_{max} = (6481 \pm 53)$ K resides in F6 spectral class and within uncertainty slips into F7; $T_{min} = (4825 \pm 25)$ K is in K0 spectral class. This implies a total range in temperature of (1656 ± 28) K. Without consideration of interstellar extinction, (B-V) magnitude (range 0.48(1) - 0.97(1)) is larger or 'redder' than expected; this explains why spectral class is cooler than we anticipate.

APPENDIX N GAIA DR2 PHYSICAL PARAMETERS

Ambiguities are rife in the *Gaia DR2* catalogue. It is not explicit in how it treats measurements of variable stars, nor does it display tailored errors in luminosity, radius or temperature for individual targets. Reference [46] suggests typical errors of $\pm 15\%$ in L , $\pm 10\%$ in R , and ± 324 K in T_{eff} . Still, it is unclear whether these parameters are measured at minimum light, maximum light, or represent some phase-averaged value. Reference [46] also mentions the potential for further systematic uncertainty. Moreover,

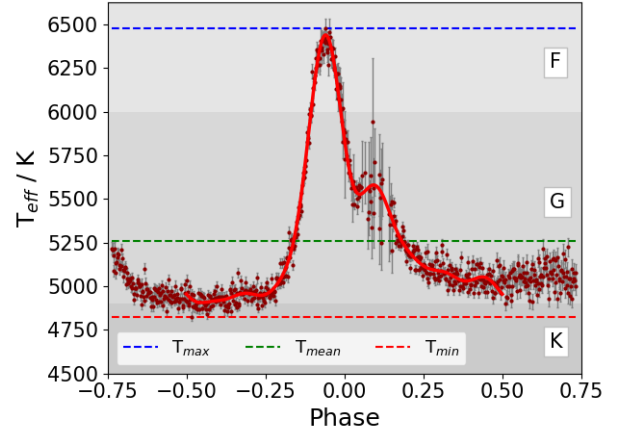


FIG. 27: The red fit-line is employed *only* to determine mean temperature from phase -0.5 to 0.5. In fitting points we have choice in number of modes and data points to fit. In some cases, a bump in the best fit-line emerges near noisy data points. On balance, we consider this is unphysical, and so we show preference to fit-line as in Fig. 26. In any case, mean temperature differs by only $\sim \pm 10$ K for various choices of mode number. This is within experimental uncertainty of what is calculated in Fig. 26, thus this discrepancy can be ignored.

the Blazhko effect is not mentioned, and we don't know when in the Blazhko cycle these observations were made.

TABLE IV: *Gaia DR2* results, associated uncertainties, and uncertainties we have inferred from reference [46]. Only parallax error is explicitly given in *DR2* catalogue.

Parameter	Measurement	Error	Best Value
Parallax / mas	1.2603	0.0331	$D = (793 \pm 21)$ pc
Temperature / K	4899	324	4899 ± 324
Luminosity / L_\odot	10.277	15%	10.3 ± 1.5
Radius / R_\odot	4.45	10%	4.5 ± 0.4

Finally it should be noted that reddening and extinction coefficients are not listed for AH Cam [4], suggesting this measurement was not made. Indeed, our mean *uncorrected* temperature of (5255 ± 35) K is consistent within $\sim 1\sigma$ of *Gaia* $T_{eff} = (4899 \pm 324)$ K. This heavily suggests extinction considerations have been neglected for AH Cam. Furthermore, just as we infer radius directly from luminosity and temperature, systematic uncertainties in temperature prevail if radius is calculated in this way by *Gaia* also. For interest, we follow through with Torres (2010) BC_V [5] and *uncorrected* temperature, and determine mean radius as $(4.9 \pm 0.2)R_\odot$, which is consistent with *Gaia* result of $(4.5 \pm 0.4)R_\odot$ (10% error implemented as above). As such we ignore *Gaia DR2* temperature and radius data. Additionally, the luminosity quoted value is far below RRL expectations, with typical $L \sim (30 - 60) L_\odot$ [6]. As mentioned by the authors [46], this must be systematically offset.

APPENDIX O INTERSTELLAR EXTINCTION

Useful photon information is diluted and distorted in a variety of forms from source to observer. One very important consideration (which is shown to produce significant systematic uncertainties if ignored, Fig. 13 and Fig. 26,

Appendix M) is the effect of interstellar extinction and reddening, that arises from interstellar dust.

Just as our atmosphere shows a preference for scattering higher frequency photons (creating a blue sky), so too does the interstellar medium (ISM) show a preference for high frequency photons. When the wavelength of the photon, λ , is comparable to the dust particle size, the dust particle will absorb and re-emit the photon in a random direction. Furthermore, this absorbed energy can be divided into multiple photons of lower energy. Conversely, when λ is in excess of particle size, photon is transmitted.

For these reasons, dust (and our atmosphere) emit heavily in IR (infra-red frequencies small compared to optical). IR is transmitted by dust clouds, as its interaction probability is small by comparison to optical photons. IR is emitted by dust clouds, because high energy photons are absorbed and divided.

In this sense, a blue photon that travels through the ISM is 'reddened'. Thus, it is imperative to quantify extinction: the reduction of intensity in a band, and reddening: the magnitude offset applied to (B-V). Reddening and extinction is quantified in §3.6. All information from [18][50].

APPENDIX P 03/12/18 V-BAND MODELLING

The m_V light curve from 03/12/18 is fitted with sine waves; the number of modes is determined in Fig. 28 to be 7, with the underlying philosophy that a lower number of modes is preferable, to avoid fitting too closely to noise embedded in signal. Fourier phases and amplitudes, depicted in Fig. 29, are extracted from 7-mode fit for use in empirical equations. Fourier phases must be combined as in Eq. 30.

$$\phi_{ij} = i\phi_j - j\phi_i \quad (30)$$

APPENDIX Q JURCSIK & KOVÁCS COMPATIBILITY AND ERRORS

The compatibility test created by Jurcsik & Kovács is designed to quantify how suitable empirical equations are for a given set of Fourier parameters. If the target deviates significantly from the sample studied in 1996 [30], empirical equations should not be applied. In calculating $[Fe/H]$ and M_V , we require ϕ_{31} , A_1 and A_3 . The deviation parameter D_F is defined as follows:

$$D_F = \frac{|F_{obs} - F_{calc}|}{\sigma_F}. \quad (31)$$

D_F is calculated for the 3 Fourier parameters we wish to employ. The equations of F_{calc} , and a Table of σ_F values are displayed.

$$\phi_{31} = 3.545 - 2.251A_1 + 3.327A_2 + 0.516\phi_{21} + 0.333\phi_{41} \quad (32)$$

$$A_1 = 0.54 + 1.054A_2 + 0.142\phi_{21} + 0.568A_3 - 0.153\phi_{31} \quad (33)$$

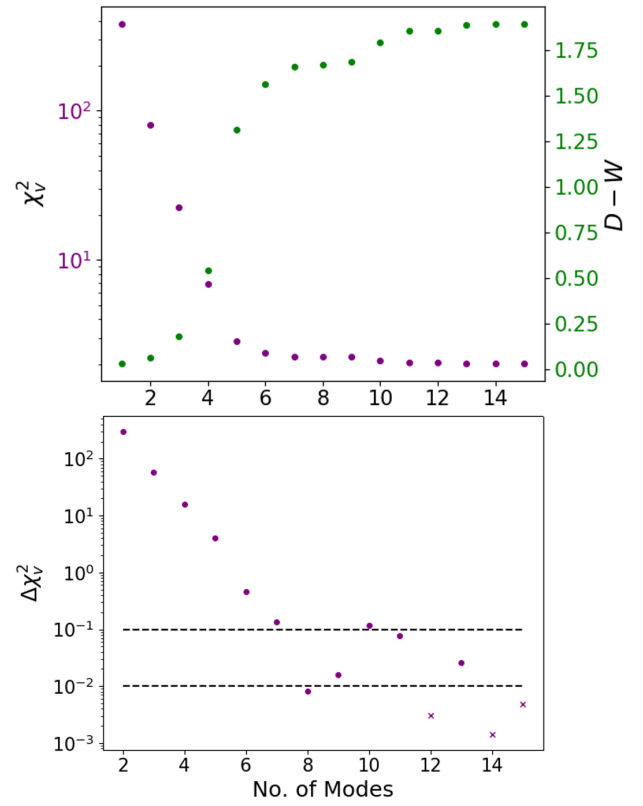


FIG. 28: The Durbin-Watson statistic, D , χ_ν^2 , and $\Delta\chi_\nu^2$ is plotted against number of fitting modes for 03/12/18 V-band light curve. 7 modes are chosen to describe the observational data. Lower plot shows 7 modes is a 'significant' improvement (as defined in Fig. 10). Although D and lower plot show 10/11 modes is an improvement to fit, it is noted that preceding this, fit quality worsens. It is presumed fit improves only to noise, and not observational signal. Upon visual inspection of fit and residuals also (Fig. 14) we deem 7 modes to be sufficient.

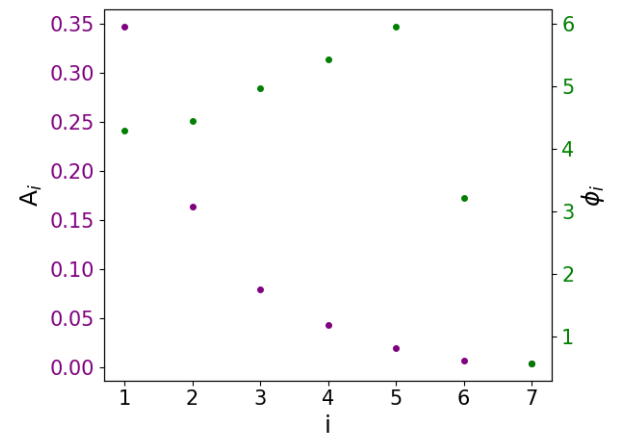


FIG. 29: Fourier Amplitudes and Phases employed from §3.5 onwards are displayed for 7-mode fit of 03/12/18 m_V observational light curve. In all cases (§3.4 and 3.5), phases are constrained to reside between 0 and 2π . In the instances where natural A_i is negative, phases are permitted an addition/subtraction of π also (given sine is an odd function).

$$A_3 = 0.005 + 0.144A_1 + 0.821A_4 \quad (34)$$

TABLE V: Standard deviations of the above 3 empirical equations for use in Eq. 31

σ	Value
ϕ_{31}	0.0462
A_1	0.0101
A_3	0.0052

The maximum D_F parameter, D_m , must be less than 3 to satisfy the compatibility test. The uncertainty, σ_{D_m} is the standard deviation of D_F values. We determine $D_m = 2.1 \pm 0.8$, just suitable for our needs. From discrepancies in convention, there are several scales of metallicity. We employ the Zinn and West (ZW) scale, and convert from the JK scale using Eq. 35 [40]. Uncertainties provided in reference [40] are propagated trivially [28]. The equation provided to determine error in metallicity is employed (Eq. 36) [40]. Fig. 30 offers a brief inspection of how the intrinsically constant metallicity is found to vary over the Blazhko phase.

$$[Fe/H]_{JK} = 1.431(\pm 0.006)[Fe/H]_{ZW} + 0.88(\pm 0.01) \quad (35)$$

$$\begin{aligned} \sigma_{[Fe/H]_{JK}}^2 &= 1.809\sigma_{\phi_{31}}^2 + 2K_{12}P + 2K_{13}\phi_{31} + 2K_{23}P\phi_{31} \\ &\quad + K_{11} + K_{22}P^2 + K_{33}\phi_{31}^2 \end{aligned} \quad (36)$$

TABLE VI: Coefficients for use in Eq. 36

K	Value
K_{11}	0.08910
K_{12}	0.00116
K_{13}	-0.01753
K_{22}	0.02529
K_{23}	-0.00289
K_{33}	0.00374

APPENDIX R APPLICABILITY OF TORRES (2010) BOLOMETRIC CORRECTIONS TO RRLS

Reddening and bolometric corrections [5] (Appendix L) yield excessively low mean luminosity and radius results, and our method is thus scrutinised. Expected luminosities are in the range $\sim(30 - 60) L_\odot$ [6] and expected M_V values are in the range $\sim(0.4 - 0.8)$ for typical RRLs [10] [31]. Just as we have employed our M_V , and yielded luminosity, we can examine the global trends of this bolometric correction system, and pose the question; Can this system replicate the expected results? Fig. 15 shows this system is inapplicable to RRLs, and we must search for a better system tailored to RRLs [45]. This result is reassuring, as L and R mean values are far from what we expect from RRLs (even if luminosity is consistent with the *Gaia DR2* catalogue, which

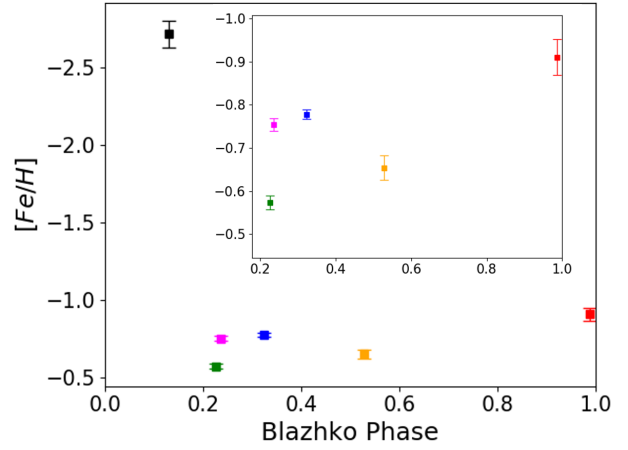


FIG. 30: Plot of $[Fe/H]_{JK}$ displays clearly that inconsistent Fourier parameters of differing Blazhko phase light curves lead to the false notion that constant physical properties such as metallicity change over time. 'Black' data point is wildly inconsistent, which is likely due to the over-fitting of light curves (upon visual inspection of this curve, 'Black' data is relatively featureless, with no RRab 'bump'). Neglecting this point, mean $[Fe/H]_{JK} = -0.73$ dex with a standard deviation of 0.1, is consistent with 'magenta' $[Fe/H]_{JK} = -0.74 \pm 0.01$, lending support to the notion that null Blazhko modulation physical parameters are a good representation of global mean physical parameters. Sinusoidal Blazhko modulation shape of peak magnitudes (Fig. 7) is not replicated by $[Fe/H]$.

is now proven to be systematically offset, Appendix N). Our temperature results are still valid. Next, for clarity, we display the unexpected results that were yielded from employing this BC system and reddening corrected temperature, in Fig. 31 and Fig. 32.

APPENDIX S RADIAL VELOCITY MODELLING

The radial velocity is derived by fitting $R(t)$ with sine waves and taking the time derivative. As is shown in Fig. 17, radius plot is very noisy, permitting too much ambiguity in sinusoidal fit. Thus we limit the phase range over which $R(t)$ is fitted in an attempt to yield low error results. Ultimately, RV curve is still dominated by errors of order $\sim 50\%$, however this is the best that can be achieved, given errors from all the data and empirical relations are compounded into the radius plot. Fig. 34 depicts how error in radius varies, and Fig. 35 determines phase range. Fig. 36 displays the RV results (The corrected results up to this point are displayed in Fig. 33).

Error in radial velocity is derived from a sum of i constituent modes, each represented as $X = A_i \omega \cos(i\omega t + \phi)$. Fractional errors in Fourier parameters $\sim 5\%$ are dominant over fractional error in ω ; 0.005%, thus ω is approximated here as a constant of zero uncertainty. Using the calculus approximation [28], error in X is derived as in Eq. 37. Following through, error contributions from all modes are added in quadrature to yield RV uncertainty.

$$\alpha_X^2 = (\alpha_A i \omega \cos(i\omega t + \phi))^2 + (\alpha_\phi A_i \omega \sin(i\omega t + \phi))^2 \quad (37)$$

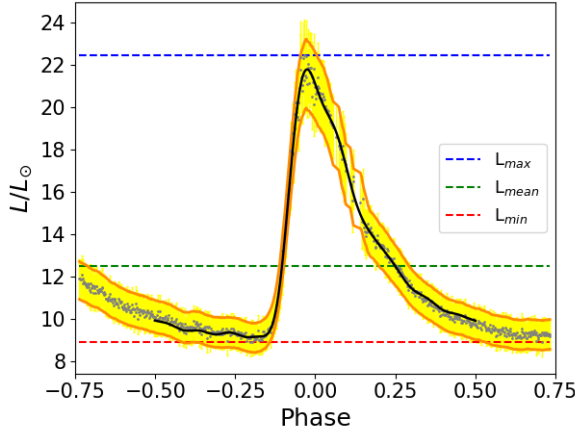


FIG. 31: Luminosity curve from 03/12/18 data, applying reference [5] bolometric corrections and reddening corrected temperature, with smoothed upper/lower error bounds [orange], and best-fit line employed for averaging [black]. Peak luminosity is offset from m_V peak time by -0.04 ± 0.03 phase. $L_{peak} = (22 \pm 2) L_{\odot}$, $L_{mean} = (12.5 \pm 0.9) L_{\odot}$, $L_{min} = (8.9 \pm 0.7) L_{\odot}$. *Gaia* quotes a luminosity of $(10.3 \pm 1.5) L_{\odot}$, where 15% error is employed as suggested in reference [46]. This is just consistent with our results, yielding weighted mean luminosity $(11.9 \pm 0.8) L_{\odot}$, near $\sim 8\%$ improvement to *Gaia* precision. This result though is far below empirical trends [6].

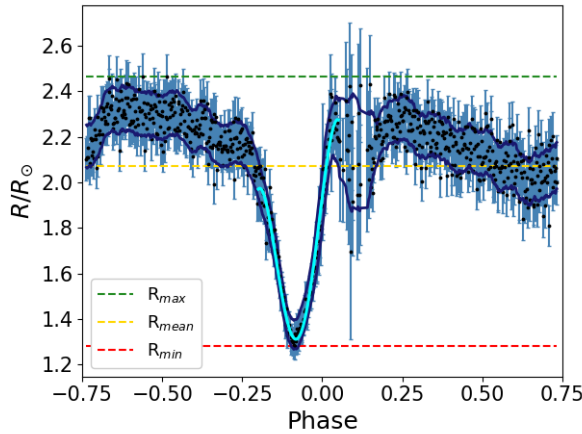


FIG. 32: Radius is plotted from 03/12/18 data, derived from Torres (2010) BC_V and reddening corrected temperature. Error contributions from temperature and luminosity plots are compounded, producing a noisy plot; typical errors $\sim 0.1 R_{\odot}$ ('smoothed' error bounds fail to encapsulate error bars for this reason). 2-mode sinusoidal fitting [cyan] is employed over low error region to model radial velocity (see Appendix S). $R_{peak} = (2.5 \pm 0.1) R_{\odot}$, $R_{mean} = (2.1 \pm 0.1) R_{\odot}$, $R_{min} = (1.28 \pm 0.06) R_{\odot}$. Without a fitting applied from phase -0.5 to 0.5, R_{mean} is calculated without accounting for uneven time spacing of data points. Minimum radius occurs at (-0.09 ± 0.03) phase. *Gaia* radius of $(4.5 \pm 0.4) R_{\odot}$ (10% error implemented [46]) is inconsistent with our results. As suggested in Appendix N, the absence of reddening considerations by *Gaia* is apparently responsible for the systematic uncertainty observed in temperature. If radius is inferred by *Gaia* from temperature, this systematic uncertainty prevails, and accounts for the inconsistency with our results.

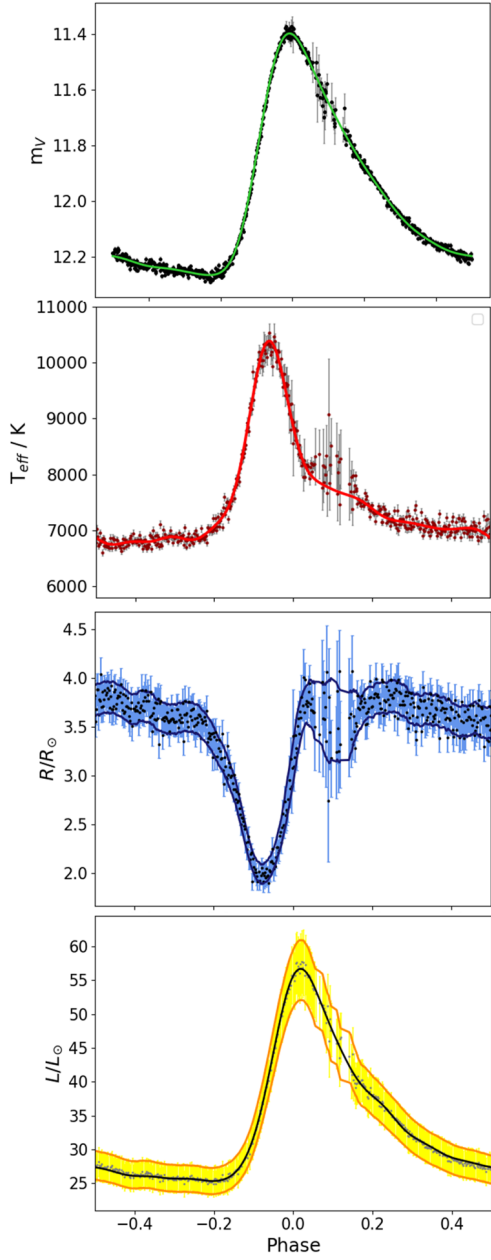


FIG. 33: Corrected m_V , T , R and L plots, see Table. X.

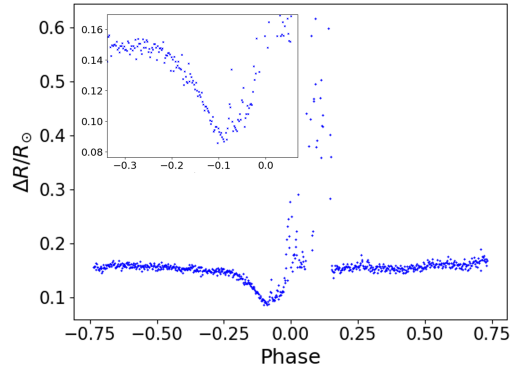


FIG. 34: The absolute uncertainty in radius from 03/12/18 is plotted. Noise compounded by propagating temperature and luminosity plots is dramatic around phase 0.1. In choosing subsection of radius plot to model radial velocity, the low error data occurs from phase $\sim (-0.25 - 0)$. Discussion is continued in Fig. 35

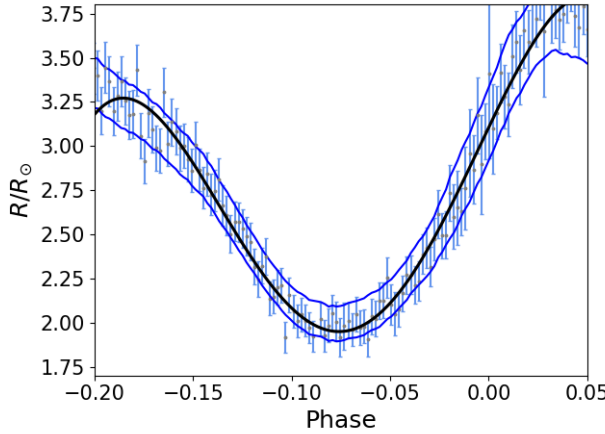


FIG. 35: The radius curve is fitted [black] from phase -0.2 to 0.05 with 2 sinusoidal modes. Free choice of phase range and number of modes is optimised, with the aim of reducing fractional errors in Fourier parameters (only these uncertainties contribute to error in radial velocity). Mean fractional error when 3 or more modes are employed exceeds 100%, whereas 2 modes yield order $\sim 10\%$ uncertainty. The ‘lips’ of the fitting at phase cut-offs are, upon visual inspection, poor representations of the data trend (particularly phase -0.2). However, these ‘lips’ are unavoidable when employing 2 modes. Thus, phase boundaries are permitted to exceed optimum range found above, such that ‘useful’ part of the graph can be extracted. Inspecting this plot, ‘useful’ portion of fitting is chosen to range (-0.175 – 0), as is consistent with findings in Fig. 34. Mean Fourier parameter fractional error is 4%, with a 3% standard deviation.

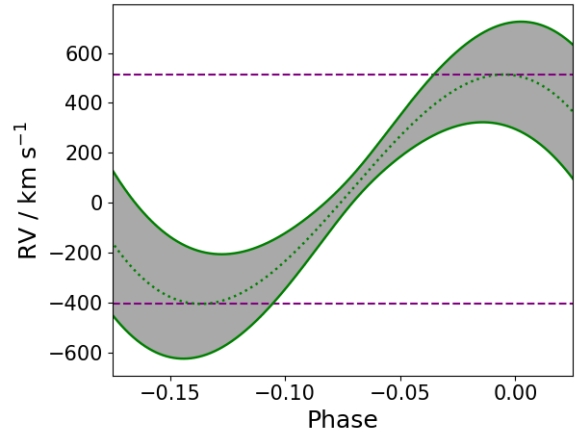


FIG. 36: Radial velocity from 03/12/18 is plotted, derived solely from Fourier parameters obtained by optimising fit of $R(t)$ low-error segment. Graph errors are substantial, ranging from $\sim \pm(55 - 300)$ km s^{-1} . $RV_{max} = (510 \pm 200)$ km s^{-1} , $RV_{min} = (-400 \pm 210)$ km s^{-1} . Error envelope shape arises from cosine fitting to RV, and profile of radius error, depicted in Fig. 33. From minimum to maximum RV, ~ 1.2 hours is elapsed. Given such large uncertainties, and results in excess of expectations by order ± 200 km s^{-1} , there is little incentive to analyse this plot further.

APPENDIX T TABLES

TABLE VII: *Gaia* parallax measurements have been converted to distance to showcase how extinction and reddening may differ between objects. Indeed, AH Cam and C2 photons travel approximately twice the distance C1 photons do, meaning it is possible light from AH Cam and C2 has experienced reddening and extinction more intensely. However, our analysis assumes all objects considered experience these effects in the same way. Systematic uncertainty here should be quantified in future work.

Target	Distance (pc)
AH Cam	793 ± 21
C1	414 ± 6
C2	835 ± 24

TABLE VIII: Peak V-band time and magnitude data from 2018 observations and 2012 Durham Archive. Companion B-band peak time observed on 03/12/18 with East-14 is consistent with V-band peak: (58455.98 ± 0.01) d. t_{peak} is in Modified HJD , transformed to HJD with the addition of 2400000.5 d.

Date	Telescope	t_{peak}	$\alpha_{t_{peak}}$	$m_{V_{peak}} (\pm \alpha_{m_{V_{peak}}})$	$\phi_{B_{peak}} (\pm \alpha_{\phi_{B_{peak}}})$	Colour
17/10/18	East-14	58409.16556	0.00384	11.16(2)	0.99(2)	Red
01/11/18	West-14	58423.89516	0.0027	11.439(9)	0.324(6)	Blue
11/11/18	East-14	58433.84388	0.00962	11.244(9)	0.227(4)	Green
14/11/18	West-14	58437.16926	0.01259	11.54(1)	0.53(1)	Yellow
21/11/18	Far-East-16	58443.80626	0.01166	11.170(9)	0.131(2)	Black
03/12/18	West-14	58455.97774	0.01215	11.38(4)	0.236(4)	Magenta
06/02/12	West-12	55963.85251	0.00586	11.23(1)	0.149(2)	-
18/02/12	East-14	55976.01477	0.00599	11.390(6)	0.255(5)	-
02/03/12	Draco	55988.92248	0.0301	11.19(1)	0.428(8)	-
05/03/12	Draco	55991.89798	0.03411	11.45(1)	0.70(1)	-

TABLE IX: Blazhko parameters from Eq. 7 derived from 2018 observational data and 2012 archive data. Final row is §3.4 case study on pulsation modelling, employing 4 peaks (Red, Blue, Green, Yellow) detailed in Table. VIII. 4-parameter fit errors in 4 peak dataset are determined as described in §3.2. Final row Blazhko period is 11.7(1); by comparison with Table. II, P_B 's are inconsistent, which is discussed in §4, as is the exceedingly low χ^2_ν .

Date	No. of Peaks	$B_0(\pm\alpha_{B_0})$	$\omega_B(\pm\alpha_{\omega_B})$	$\phi_B(\pm\alpha_{\phi_B})$	$B_1(\pm\alpha_{B_1})$	χ^2_ν
2018	6	0.20(2)	0.57(1)	4.8(2)	11.35(1)	4.54
2012	4	0.2(2)	0.571(9)	3.8(2)	11.38(3)	9.02
2018	4	0.204(7)	0.535(6)	4.25(9)	11.343(6)	0.33

TABLE X: Results of physical parameters are ordered by peak phase (where radius 'peak' is a minimum). Results replicate the κ mechanism narrative, where temperature peaks with minimum radius, and opacity decreases after expansion, causing the peak in luminosity (§3.4). Time from minimum radius to peak luminosity is (54±18) mins. In future, this time interval should be theoretically computed for AH Cam and compared. Phase zero is the m_V peak time, which is observed at 0.236 ± 0.004 phase in the Blazhko period. Typical RRL mean values of L and R are empirical, and still today there is ambiguity in defining the edges of the instability strip, thus the temperature range has potential to be extended. Mean value temperature nears the 'blue edge' of the instability strip, indicating a hot RRab. Radius is atypically small, with sources of systematic uncertainty discussed in §4. Systematic error in m_V peak time (± 0.03 phase) is ignored in peak phase errors. *Gaia* errors are taken from [46].

Property	Minimum	Mean	Maximum	Peak Phase	Typical RRL Mean	<i>Gaia DR2</i>
R / R_\odot	1.90(9)	3.4(2)	4.1(4)	-0.08(3)	4 - 6	4.45($\pm 10\%$)
T_{eff} / K	6601(52)	7523(82)	10537(166)	-0.061(4)	6500 - 7750	4899(± 324)
L / L_\odot	25(2)	34(3)	58(5)	0.018(5)	30 - 60	10.277($\pm 15\%$)

TABLE XI: Observing Log of 10 nights. FWHM column in arcseconds ('') details range, mean and standard deviation during exposures.

Date	Time	HJD(+240000.5)	Telescope	Exposures	FWHM ('')	Observing Notes
17/10/18	18 : 59 : 53 – 19 : 31 : 01	58408.79176 – 58408.81339	West-14	V 30s 49	3.1 – 5.0 3.5(4)	Few Exposures due to telescope demand from other AstroLab Students.
17/10/18	20 : 35 : 10 – 05 : 57 : 45	58408.85793 – 58409.18209	East-14	V 30s 1017	2.6 – 9.5 5(2)	Peak was observed. Good observing conditions. Light curve 'shoulder' not visible.
18/10/18	18 : 35 : 12 – 19 : 54 : 21	58409.76001 – 58409.82879	West-14	B 90s 50	3.5 – 8.1 4.5(8)	Data is not useful. Frames yielded to determine optimum B-band exposure time (60s).
18/10/18	21 : 31 : 05 – 05 : 52 : 42	58409.89694 – 58410.22537	West-14	V 60s 438	2.4 – 8.5 5(1)	35 points excluded due to failed astrometric fitting. Otherwise, low error data but no peak observed.
21/10/18	21 : 02 : 53 – 05 : 52 : 42	58412.87736 – 58413.24481	West-14	B 60s 462	0.9 – 8.2 4.7(8)	Peak is well defined, but data cannot be phase folded due to Blazhko effect.
22/10/18	17 : 05 : 30 – 18 : 15 : 15	–	West-14	Dark 144	–	32 dark frames each in B & V at 0.03s 16 dark frames in V for (0.2, 1, 4, 15, 60)s.
24/10/18	21 : 54 : 03 – 04 : 24 : 20	58415.91271 – 58416.18375	Draco2	V 30s 705	1.1 – 7.3 5.0(7)	82 points excluded due to failed astrometric fitting. Peak observed but too noisy to analyse accurately.
01/11/18	20 : 15 : 36 – 05 : 52 : 02	58423.84435 – 58424.24465	West-14	V 30s 891	2.7 – 6.1 4.0(6)	Excellent Data with well defined peak. Light Curve shoulder is clearly visible.
11/11/18	18 : 31 : 53 – 03 : 58 : 48	58433.77232 – 58434.16601	East-14	V 30s 1024	2.9 – 7.0 4.7(8)	Magnitude errors are large at peak and on descent. Error in peak time is large: 0.00962d.
14/11/18	19 : 11 : 07 – 05 : 51 : 37	58436.79957 – 58437.24436	West-14	V 30s 990	1.1 – 8.0 3.9(5)	Peak is well defined, however light curve shoulder is very noisy.
21/11/18	17 : 26 : 35 – 00 : 37 : 28	58443.76454 – 58444.01116	Far-East-16	V 30s 697	1.3 – 12.3 3.2(6)	Data is low error except unfortunately around peak time; error of 0.01166d
21/11/18	18 : 37 : 00 – 19 : 53 : 04	58443.78127 – 58443.82814	Draco2	B 60s 69	3.2 – 7.3 4.1(8)	Attempt to yield a simultaneous B-V exposure. Demand from students prevent long enough exposure.
03/12/18	16 : 56 : 24 – 05 : 42 : 41	58455.70601 – 58456.23815	West-14	V 30s 1184	0.7 – 8.4 3.4(5)	Simultaneous B and V exposures. During hrs 7-8 data is noisy. Peak errors order ± 0.02 mag.
03/12/18	16 : 56 : 23 – 05 : 53 : 18	58455.70618 – 58456.2479	East-14	B 60s 740	0.7 – 9.4 5(1)	Difference in BV peak times is (0.00 ± 0.02) d; Consistent with simultaneous t_{peak} in all bands.